ABSTRACT

Title of Thesis: AN ASSESSMENT OF AEROGRAVITY-ASSISTED TRAJECTORIES FOR AEROCAPTURE AT THE ICE GIANTS

Grace Zimmerman
Master of Science, 2023

Thesis Directed by: Dr. Christine Hartzell
Department of Aerospace Engineering

The Ice Giants, Neptune and Uranus, are two candidates for an aerocapture maneuver, in which a spacecraft is captured into a bound orbit through a single atmospheric pass. Another aeroassisted maneuver, the aerogravity-assist (AGA), uses an atmospheric pass to increase the turn angle about a planet, thus enabling large changes in a spacecraft's heliocentric velocity. Both maneuvers require high arrival velocities and thermal protection system technologies; thus, it may be beneficial to execute both maneuvers on a single mission. To investigate the possible benefit of an AGA trajectory for setting up an aerocapture maneuver at the Ice Giants, a two-layer optimization approach has been employed to investigate the trajectory space. As an AGA maneuver relies on minimal planetocentric velocity loss due to drag, previous studies have focused on AGAs with high lift-to-drag ratio (L/D) vehicles, despite all heritage interplanetary vehicles being low-L/D. Due to the technology barrier for high-L/D interplanetary vehicles, the present study uses lower L/D vehicles, from low-L/D heritage vehicles to mid-L/D optimally-shaped ve-

hicles. Feasible trajectories are identified for both Uranus and Neptune that increase the number of feasible launches as compared to traditional gravity-assisted (GA) trajectories. In addition, the study identifies a new family of periodic high-altitude AGA trajectories to Uranus that are feasible using heritage vehicles. For Uranus, trajectories are identified that enable aerocapture within current heat shield technology constraints using a vehicle with L/D = 1.25.

AN ASSESSMENT OF AEROGRAVITY-ASSISTED TRAJECTORIES FOR AEROCAPTURE AT THE ICE GIANTS

by

Grace Zimmerman

Thesis submitted to the Faculty of the Graduate School of the
University of Maryland, College Park in partial fulfillment
of the requirements for the degree of
Master of Science
2023

Advisory Committee:
Dr. Christine Hartzell, Chair/Advisor
Dr. David Akin
Professor Brent Barbee

Acknowledgments

The study would like to acknowledge the support of the National Science Foundation's Graduate Research Fellowship Program.

Table of Contents

List of Tables

List of Figures

Nomenclature

E	vehicle lift-to-drag ratio
C_l	vehicle lift coefficient
C_d	vehicle drag coefficient
S	vehicle surface area, m^2
ρ	atmospheric density, kg/m^2
a	altitude km
z	atmospheric scale height, km^{-1}
m	vehicle mass, kg
V_∞^-	hyperbolic excess speed at arrival, km/s
V_∞^+	hyperbolic excess speed at departure, km/s
V_{s_i}	heliocentric velocity at arrival
V_{s_f}	heliocentric velocity at departure
θ_{atm}	planetocentric atmospheric turn angle
β	vehicle ballistic coefficient, kg/m^2
μ	gravitational constant, km^3/s^2
q_c	convective heating rate, W/cm^2
α	angle between the planet's velocity vector and the hyperbolic excess velocity at arrival km/s
ϵ	angle between the planet's velocity vector and the hyperbolic excess velocity at departure km/s
λ	costate variables

Subscripts

$*$	maximum vehicle lift-to-drag ratio
s	heliocentric reference
ref	w.r.t. atmospheric reference altitude

Chapter 1: Introduction

1.1 Motivation for Ice Giant Missions

The Ice Giants have only been visited by the Voyager II spacecraft during brief flybys in the 1980s, despite the scientific intrigue of both planets. The planets themselves are poorly understood, as models predict a small number of these Ice Giants in solar system evolution, and yet, many of the newly-discovered exoplanets are of Ice Giant size. A dedicated mission to one of the Ice Giant planets would improve understanding of Ice Giant evolution and formation, as well as solar system evolution as a whole. The importance of a flagship mission to the Ice Giants has been highlighted in the two most recent Planetary Science Predecadal Surveys. The 2012 survey lists a Uranus Orbiter and Probe as one of five recommended flagship missions [1], and the same mission was listed as the highest-priority in the 2023 survey [2].

1.2 Aeroassisted Maneuvers

1.2.1 Aerocapture

Aerocapture is the process of entering a bound orbit about a planet by utilizing the drag force to decrease the orbital energy during a single pass through the planet's atmosphere. The maneuver is attractive for many interplanetary missions, and has recently been an item of invest-

ment by NASA's Space Technology Mission Directorate (STMD) due to the possible applications to Martian missions.

There are multiple potential benefits of using aerocapture for an interplanetary mission. The maneuver requires a high V_∞ at arrival which lends itself to short mission time-of-flights. As outer-planetary mission velocities are often limited by the propulsive ΔV capabilities, a non-propulsive maneuver like aerocapture could reduce overall mission times and allow for additional launch opportunities. Aerocapture also allows for larger mass delivery to the mission targets, as the propulsive ΔV requirements are greatly reduced. This allows for further instrumentation and other payloads on missions.

The aerocapture maneuver requires a vehicle with a sufficiently large L/D-ratio. As all flight-tested interplanetary vehicles are blunt-body vehicles, which are typically constrained to a L/D-ratio of 0.3 and under, aerocapture could require technology past current readiness level. In addition, the maneuver requires sufficient aerothermodynamic protection in the form of thermal protection systems.

The Ice Giants serve as two candidates for aerocapture as missions to the outer planets face challenges due to large time-of-flights and orbital capture requirements. Previous aerocapture studies have suggested that the maneuver could reduce the overall mission time-of-flight to the Ice Giants by 2-5 years, demand less intensive launch vehicles, and maximize delivered mass by up to 40% [3]. In addition, performing an aerocapture maneuver at the Ice Giants allows for less reliance on propulsive methods to perform the orbital insertion ΔV, thus increasing the number of feasible mission opportunities.

1.2.2 Aerogravity-Assist

Within the same family of aeroassisted maneuvers is the aerogravity assist. Similar to traditional gravity assists (GA), the aerogravity assist (AGA) uses an atmospheric flyby of a planet to increase the spacecraft's heliocentric velocity. The increase in heliocentric velocity during a GA is defined by the turn angle about the planet, which is limited by the radius of closest approach. Typically this radius is constrained by the atmospheric height; however, in an AGA maneuver, the vehicle dips into the planetary atmosphere, lowering the radius of closest approach and thus increasing the spacecraft's heliocentric velocity.

Although the GA has been used extensively in interplanetary mission design, the AGA is a relatively new, untested concept. One of the first in-depth studies on the potential of aerogravity assists was performed by McRonald and Randolph in 1990 [4], with subsequent decades of research following the initial study. Such studies showed aerogravity assists to be particularly advantageous for missions to the outer planets, such as the Ice Giants; Sims, et al. demonstrated that a Uranus or Neptune mission utilizing a Venus-Mars AGA could have a interplanetary time of flight (TOF) as low as 3.17 and 4.25 years, respectively, with a high-L/D vehicle [5]. This is a substantial reduction in the typical 12-15 years estimated for missions with chemical propulsive and GA methods [3].

The main challenge in an AGA is in minimizing planetocentric velocity loss due to atmospheric drag. Typically, this is addressed by using a high lift-to-drag ratio (L/D) vehicle, such as a waverider [6]. As these vehicles are currently at a low technology readiness level, it is advantageous to try and minimize the required L/D for a successful AGA maneuver. In addition, AGAs with heritage vehicles have not been fully investigated in previous AGA studies. With

these factors in mind, it is of importance to consider both heritage vehicles and low-to-mid-L/D vehicles in AGA trajectories.

Both aerocapture and AGAs require thermal protection systems to protect the spacecraft from heating due to atmospheric drag. As both maneuvers require this subsystem, it is natural to investigate the possibility of utilizing inner solar system AGAs to set up for a high velocity aerocapture maneuver at the Ice Giants. By utilizing inner solar system AGAs, there exist more launch opportunities, as the inner solar system planets have much faster orbital periods and alignments for AGAs when compared to typical gas giant GAs.

1.3 Study Purpose

The following study uses a two-layer optimization approach to identify interplanetary trajectories using inner solar system AGAs that enable aerocapture at the Ice Giants. An outer layer surrogate optimization method is utilized to determine minimum convective heating rates and minimum Earth launch energy requirements over the feasible trajectories. A two-point boundary value problem serves as the indirect optimization method of the inner layer for finding the atmospheric trajectory of the AGA that minimizes spacecraft energy loss due to drag.

In addition, to reduce the technology development necessary for AGAs, the study considers a variety of lower-L/D vehicles as compared to current literature. As AGAs are typically performed to maximize final heliocentric velocities over traditional GAs, previous studies tend to utilize vehicles with L/D ratios greater than 3. The present study uses optimally-shaped vehicles with L/D ratios from 0.25 to 3 as well as heritage vehicles with L/D ratios less than 0.3.

Chapter 2: Methodology

A mission to the Ice Giants with solely inner solar system AGAs will have an interplanetary flight time dominated by the TOF from the last AGA planet to the arrival Ice Giant planet. As this TOF defines the possible AGA geometries for a given mission, the present study propagates the trajectories backwards, starting with an Ice Giant arrival date and spacecraft arrival state. Using velocity matching and spacecraft state constraints imposed by the aerocapture requirements, an AGA trajectory to the Ice Giant planet is found.

2.1 Interplanetary Trajectory Search

The program for the interplanetary trajectory search serves as the objective function of the outer layer optimization method. The objective function for an optimization method calculates the value to maximize or minimize, using a set of input design variables. In the present study, the objective function is the Interplanetary Trajectory Program, outlined in detail below, while the objective function's output is set to be either $q_{c_{max}}$ or $C3$.

Interplanetary Trajectory Program

1: **Input:** Ice Giant Planet, Ice Giant Arrival Date, Spacecraft Arrival Hyperbolic Excess Velocity (V_∞^-), Vehicle Choice, Array of AGA Planets (agaPlanetsArray), Objective Function Output Choice ($q_{c_{max}}$ or $C3$)
2: Grab Ice Giant Planet ephemeris data for the Ice Giant Arrival Date
3: Set variable k = length(agaPlanetsArray)
4: Grab range of AGA Planet k ephemeris data from 3 to 10 or 14 years, for Uranus and Neptune, respectively
5: Calculate Lamberts Solution for each ephemeris from AGA Planet k to the Ice Giant Planet until the V_∞^- is matched
6: **while** AGA Planet $k \neq$ agaPlanetsArray(1)
7: Grab range of AGA Planet $k-1$ ephemeris data from 1 month to 2 years before AGA planet k arrival date
8: Calculate Lamberts Solution for each ephemeris from AGA Planet $k-1$ to AGA Planet k, matching solutions with the velocity calculated by step 5
9: Calculate range of atmospheric turn angles about the AGA planet k using interplanetary trajectory variables from step 8
10: Calculate set of AGA maneuvers using the two-point boundary value problem, with boundaries given by interplanetary trajectory variables from step 8
11: Determine best AGA maneuver based on input Objective Function Variable Choice
12: $k = k-1$
13: **end**
14: Grab range of ephemeris data for Earth 1 month to 2 years before AGA $k-1$
15: Calculate Lamberts Solution for each ephemeris from Earth to AGA Planet $k-1$, matching solutions with the velocity calculated by step 11
16: Calculate set of atmospheric turn angles about the AGA Planet $k-1$ using interplanetary trajectory variables from step 15
17: Calculate set of AGA maneuvers, with boundaries given by interplanetary trajectory variables from step 15
18: Determine which AGA maneuver is best based on input Objective Function Output Choice
19: **Output:** Calculated Objective Function Output ($q_{c_{max}}$ or $C3$)

A fast Type II Lamberts Solution developed by Izzo [7] is employed to find the sets of possible trajectories between planetary destinations that match velocity requirements. Both the long and short path solutions to the given Lamberts problem are investigated as potential trajectories.

The atmospheric turn angle for the AGA maneuver is calculated through the following equations:

$$\theta_{atm} = 2\pi - (\pi - \phi + (f_\infty^+ - f_{dep}) + (f_\infty^- - f_{arr})) \tag{2.1}$$

Where the interplanetary variables are calculated assuming the radius of closest approach is equal to a reference radius, R_{ref}:

$$h_\infty = R_{ref}|V_\infty| \qquad e_\infty = \frac{|V_\infty|^2 R_{ref}}{\mu} - 1 \qquad f_\infty = acos(\frac{-1}{e_\infty}) \tag{2.2}$$

The V_∞ vectors are calculated as the difference of the Lamberts solution and the AGA planet velocity. The planetocentric interplanetary variables are given by:

$$h = R_{ref}|V| \qquad e = \frac{|V|^2 R_{ref}}{\mu} - 1 \qquad f = acos(\frac{\frac{h^2}{R_{atm}\mu} - 1}{e}) \tag{2.3}$$

Where V, the planetocentric velocity at atmospheric entry and exit, is calculated by the two-body conservation of energy equation:

$$V = (\frac{2\mu}{R_{atm}} + |V_\infty|^2)^{\frac{1}{2}} \tag{2.4}$$

Finally, the angle between the incoming and outgoing V_∞ vectors, ϕ, is calculated using the inner product of the two vectors. This represents the total turning angle between the V_∞ vectors.

As the AGA maneuver rotates the line of apsides, the outgoing V_∞ vector is not equal to the incoming V_∞ vector, unlike a traditional GA. The final heliocentric velocity after the AGA maneuver must be calculated using the interplanetary trajectory variables:

$$
\begin{aligned}
\beta_{s_i} &= acos(\frac{V_p V_{s_i}}{|V_p||V_{s_i}|}) \\
\alpha &= asin(\frac{V_i sin(\beta_{s_i})}{|V_\infty^-|}) \\
\epsilon &= \pi - \phi - \alpha \\
V_{s_f} &= ((V_p + |V_\infty^+|cos(\epsilon))^2 + (V_\infty^+ sin(\epsilon))^2)^{\frac{1}{2}}
\end{aligned}
\tag{2.5}
$$

Where V_p is the heliocentric velocity of the AGA planet.

To ease the computational requirements for the trajectory search process, TOF constraints of 10 and 14 years for Uranus and Neptune, respectively, are placed on the last leg of the interplanetary flight. The interplanetary TOF in the inner solar system portions of the mission are constrained from 30 days to 2 years. In addition, only maneuvers with an altitude of closest approach less than 150km are considered, to ensure the program only finds AGA solutions. The 150km altitude is within the atmosphere for each AGA planet. The program also enforces a launch energy constraint of $< 150\ km^2/s^2$ to account for current launch vehicle capabilities [8].

Within the optimization solver, specific constraints are imposed for the design variables. For arrival at the Ice Giant planet, the solver searches from the minimum theoretical corridor width (TCW) velocity requirement to 5 km/s over the minimum TCW requirement. The TCW defines the range of flight path angles that result in successful aerocapture, thus providing an estimation metric for the aerocapture maneuver. Additionally, the solver has the ability to consider any combination of AGAs during its interplanetary trajectory. For the current study, all inner solar system planets with atmospheres are considered as candidates for AGAs.

As the surrogate optimization function used in the study does not explicitly converge on non-continuous objective functions [9], such as the current trajectory search program, a stopping

criterion must be defined. For a one-month search period, the stopping criterion is set at 250 function evaluations. At 250 function evaluations each iteration of the optimizer, using the same input design variables, yields identical global optimum solutions, indicating that the stopping criterion is sufficient.

2.2 Two-Layer Optimization Approach

The outer layer of the two-layer optimization approach is composed of a surrogate optimizer, chosen due to the costly computation times associated with trajectory searches, as well as the solver's global optimum solution capabilities. Surrogate optimization allows for an approximation of the function evaluation, the minimum of which is then used to estimate the minimum of the exact function evaluation. MATLAB's surrogateopt() function, of the Global Optimization Toolbox [10], is used to find the global minimum of the objective function output variable, set as either the Earth launch energy or the maximum convective heating rate during the AGA maneuver(s). The surrogateopt() functionality additionally supports both double and integer values for its design variables, further simplifying the optimization process when considering dates and AGA planet combinations.

A series of checkpoints were created to ease the outer layer optimization throughout the Interplanetary Trajectory Program. Following each Lambert and AGA solution, an evaluation is performed to ensure calculation success and variable constraint maintenance. If no viable solution was found, the trajectory solution program quits and returns a value scaled to the number of successful Lamberts and AGA solutions from the current iteration. This method allows for optimization feedback with infeasible trajectories, which continues pushing the surrogate optimizer

towards the optimal trajectory solution.

The inner layer is an indirect optimization approach in the form of a two-point boundary value problem (TPBVP) used to solve for the atmospheric trajectory that results in the largest final spacecraft heliocentric velocity. This layer lies within the previously-outlined Interplanetary Trajectory Program. For each function evaluation in the outer layer, the inner layer optimization approach ensures the AGA maneuver is optimal based on the AGA's heliocentric ΔV. The derivation for the AGA TPBVP is detailed in following sections.

2.3 Aerogravity-Assist Modeling

Following the approaches of Henning, et al. [11] and Lohar, et al. [12], a two-point boundary value problem is constructed to calculate the atmospheric trajectory that maximizes the final heliocentric velocity.

2.3.1 Atmospheric Planar Equations of Motion

The optimal AGA solution is first defined by the planar equations of motion around a nonrotating planet [13]:

$$\begin{aligned}
\frac{dr}{dt} &= V sin\gamma \\
\frac{d\theta}{dt} &= \frac{V cos\gamma}{r} \\
\frac{dV}{dt} &= \frac{-V^2 \rho S C_d}{2m} - \frac{\mu}{r^2} sin\gamma \\
\frac{d\gamma}{dt} &= \frac{V \rho S C_l}{2m} - (\frac{\mu}{V r^2} - \frac{V}{r}) cos\gamma
\end{aligned} \tag{2.6}$$

Where r = the radial distance of the spacecraft from the center of the planet, t = time, V

= spacecraft planetocentric velocity, γ = the spacecraft planetocentric flight path angle, ρ = atmospheric density, S = the spacecraft surface area, m = spacecraft mass, μ = the gravitational parameter of the planet, and C_l and C_d represent the spacecraft lift and drag coefficient, respectively. From these equations, the dependence on the time variable can be eliminated, as it is not of importance in the current approach. Instead, the first-order derivatives can be restructured to have θ as the independent variable, as θ will become a future boundary condition. In addition, the equations of motion are nondimensionalized to ease computation.

$$\begin{aligned} \frac{d\tilde{r}}{d\theta} &= \tilde{r}tan\gamma \\ \frac{dV}{d\theta} &= \frac{-\tilde{\rho}\tilde{V}\tilde{r}\zeta\tilde{C}_d}{E^*cos\gamma} - \frac{2tan\gamma}{\tilde{r}} \\ \frac{d\gamma}{d\theta} &= \frac{\tilde{\rho}\zeta\tilde{r}\tilde{C}_l}{2cos\gamma} - \frac{1}{\tilde{r}\tilde{V}} + 1 \end{aligned} \tag{2.7}$$

Where the nondimensionalized variables are:

$$\tilde{r} = \frac{r}{R_{ref}} \qquad \tilde{V} = \frac{V^2 R_{ref}}{\mu} \qquad \tilde{\rho} = exp[-(1/z)R_{ref}(\tilde{r}-1)] \tag{2.8}$$

$$\tilde{C}_l = \frac{C_l}{C_l^*} \qquad \tilde{C}_d = \frac{C_d}{C_d^*} \tag{2.9}$$

C_l^* and C_d^* correspond to the lift and drag coefficient at the maximum lift-to-drag ratio, E^*, and z represents the planet's scale height. To supplement the previous equations, the variable ζ is defined:

$$\zeta = \frac{\rho_{ref} S C_l^* R_{ref}}{2m} \tag{2.10}$$

In the current setup, the vehicle exercises lift modulation in the form of the lift coefficient

C_l. As the equations of motion considered are planar, the bank angle is excluded from the current setup. Instead, the C_l value is allowed to be negative and positive, which correlates directly to the vehicle's bank angle; a negative C_l represents the spacecraft flying upside down, which corresponds to a bank angle of 180°, whereas the positive C_l represents a normal flight, corresponding to a bank angle of 0°. The present study restricts the spacecraft's degrees of freedom in order to simplify the calculations and make an overall estimate of the interplanetary trajectory options.

2.3.2 Aerodynamic Model

A drag polar model is used to estimate the L/D of the spacecraft throughout the atmospheric trajectory, where the normalized drag coefficient is modeled as:

$$\tilde{C}_d = \frac{n-1}{n} + \frac{\tilde{C}_l^n}{n} \tag{2.11}$$

Where n is a function of the Mach number. The drag polar values of n = 1.5 and n = 2 represent the hypersonic and subsonic regimes, respectively. Despite the hypersonic nature of AGAs, many recent studies have used the parabolic n = 2 drag polar for their computations [11, 14, 15]. Henning et al [11] proved that the two models produce very similar results, with the only difference being a slight deviation in the upper atmosphere that does not lead to substantial aerodynamic effects. In addition, the n = 1.5 TPBVP solution is heavily reliant on the TPBVP initial guess, whereas the n = 2 solution does not have this dependence. With these factors in mind, for the purpose of this study the drag polar is set at n = 2.

In addition, an exponential density model is used to simulate the atmospheric density during the AGA. For the trajectory solution process, the planetary atmospheric variables used are

outlined in Table 2.1.

Table 2.1: Atmospheric Variables for AGA Solution

Planet	$a_{ref}(km)$	$\rho_{ref}(kg/m^3)$	**z** (km^{-1})	C_l^*
Venus	63	0.5	0.17	0.034
Earth	70	8e-5	0.117	0.02
Mars	28	3e-3	0.094	0.015

The reference altitudes for each AGA planet are dictated by the lift coefficient at the vehicle's maximum L/D ratio, C_L^*. According to Anderson [6], for optimally-shaped vehicles, lift coefficients of 0.015 and 0.034 are expected at Mars and Venus, respectively. These optimally shaped vehicles are expected to achieve the smallest amount of velocity loss due to drag at altitudes of 28 km at Mars and 63 km at Venus. An estimate of C_L^* and reference altitude for Earth AGAs is made following the same optimally-shaped vehicle guidelines [6]. At Mach 26, the C_L^* can be estimated as 0.02 at a reference altitude of 70 km. [16].

During atmospheric flight, a vehicle will experience both convective and radiative heating. As the convective heating dominates the total heat rate at mid- to high-atmospheric altitudes, the present study will consider only the convective heat rate during optimization.

To generate an estimate of the heat rate on the spacecraft during the AGA maneuver, a convective heating rate q_c is calculated throughout the atmospheric flight according to the equation:

$$q_c = k\sqrt{\frac{\rho}{r_n}}V^3 \tag{2.12}$$

Where ρ is the atmospheric density in kg/m^3, r_n is the vehicle nose radius, V is the vehicle's planetocentric velocity in m/s, and k is the Sutton-Graves constant in $\sqrt{kg}/m$. For the

optimally-shaped vehicles, r_n is set at 1 meter. In addition, the Sutton-Graves constant is estimated as 1.9027e-08 $\sqrt{kg}/m$ for Mars, 1.7415e-08 $\sqrt{kg}/m$ for Earth, and 1.8960e-08 $\sqrt{kg}/m$ for Venus [17, 18].

2.3.3 Two-Point Boundary Value Problem

Again following the approach of Lohar [12] and Henning [11], the optimal trajectory is solved using a TPBVP where the objective function is defined as:

$$J = V_{s_f} \tag{2.13}$$

Which is further defined in Equation 2.5.

Although the cost function has been set as the minimum spacecraft heat load in previous studies, including that of Edelman, et al [19], the present study looks to maximize the heliocentric velocity after the maneuver to ensure maximum performance from the lower-L/D vehicles. The minimum convective heating is instead considered in the outer-layer of the two-layer optimization approach.

The Hamiltonian can be constructed using the previously defined planar equations of motion:

$$\begin{aligned} H &= L + \lambda^T f \\ &= \lambda_r(\tilde{r}tan\gamma) - \lambda_u[\frac{\tilde{V}\zeta\tilde{r}\tilde{C}_d}{E^* cos\gamma}\tilde{\rho} + \frac{2tan\gamma}{\tilde{r}}] + \lambda_\gamma(\frac{\zeta\tilde{r}\tilde{C}_l}{2cos\gamma}\tilde{\rho} - \frac{1}{\tilde{r}\tilde{V}} + 1) \end{aligned} \tag{2.14}$$

The optimal control law can then be computed by determining the costate equations from the Euler-Lagrange theorem:

$$\frac{d\lambda_r}{d\theta} = -\frac{\partial H}{\partial \tilde{r}} \qquad \frac{d\lambda_V}{d\theta} = -\frac{\partial H}{\partial \tilde{V}} \qquad \frac{d\lambda_\gamma}{d\theta} = -\frac{\partial H}{\partial \gamma} \tag{2.15}$$

For the present study, the control mechanism is in lift modulation, where the vehicle can vary its angle of attack through the lift coefficient C_l. Ultimately, the control law is determined by setting ∂H / $\partial \tilde{C_l}$ = 0 with the drag polar constant n = 2, and subsequently solving for $\tilde{C_l}$:

$$\tilde{C_l} = \frac{E^* \lambda_\gamma}{2\tilde{V}\lambda_V} \tag{2.16}$$

As there are three costates within the optimization process, it is beneficial to define a new variable as the ratio between two costates, thus reducing the number of required costates definitions:

$$C_5 = \frac{\lambda_r}{\lambda_V} \tag{2.17}$$

Finally, the differentials of C_5 and $\tilde{C_l}$ are derived with respect to θ and the planar equations of motions can be substituted to obtain the following costate differential equations:

$$\frac{d\tilde{C_l}}{d\theta} = \frac{\tilde{r}\zeta sin\gamma(1-\tilde{C_l}^2)}{4cos^2\gamma}\tilde{\rho} - \frac{\tilde{r}E^*C_5}{2\tilde{V}cos^2\gamma} + \frac{E^*}{\tilde{V}\tilde{r}cos^2\gamma} + \frac{2\tilde{C_l}tan\gamma}{\tilde{V}\tilde{r}} + \frac{2\tilde{C_l}^2}{\tilde{V}\tilde{r}E^*}$$

$$\frac{dC_5}{d\theta} = -C_5 tan\gamma + \frac{\tilde{V}\zeta(1+\tilde{C_l}^2)(1-\tilde{r}\frac{1}{z}R_o)}{2E^*cos\gamma}\tilde{\rho} - \frac{2tan\gamma}{\tilde{r}^2} - \frac{2\tilde{C_l}}{\tilde{r}^2E^*} - \frac{\tilde{V}\zeta\tilde{C_l}^2(1-\tilde{r}\frac{1}{z}R_o)}{E^*cos\gamma}\tilde{\rho}$$
$$- \frac{\tilde{r}\zeta C_5(1+\tilde{C_l}^2)}{2E^*cos\gamma}\tilde{\rho} + \frac{2\tilde{C_l}C_5}{\tilde{V}\tilde{r}E^*} \tag{2.18}$$

Using the set of five differential equations outlined in Eqns (7) and (16), the TPBVP can be solved using the previously-calculated θ_{atm}.

2.4 Vehicle Study

To prepare for the evaluation of aerogravity-assisted trajectories to the Ice Giants, a literature search was conducted to catalogue the ballistic and aerodynamic characteristics of various heritage vehicles. This included vehicles with recorded aerodynamic characteristics, such as the Apollo Command and Service Module (CSM) [20], and vehicles with interplanetary flights and limited aerodynamic data, such as the Mars Exploration Rover Entry Capsule [21]. A number of heritage vehicles have recorded ballistic coefficients, surface areas, and masses, but lack a recorded maximum lift-to-drag ratio. For the purpose of this study, the maximum-L/D for heritage vehicles without a flight-tested maximum-L/D was estimated at 0.2, which falls within the range of low-lift-to-drag vehicles (< 0.3).

In addition, optimally-shaped vehicles with reduced L/D ratios were considered, beginning with the vehicle outlined by Henning, et al. [11]. To further expand upon the reliance of L/D on the atmospheric flight, a number of vehicles were defined to represent the same optimally-shaped vehicle outlined in Henning et al., but with reduced L/D and ballistic coefficients. All optimally-shaped vehicles followed the Henning et al. [11] mass-to-area ratio of 100 kg/m^2.

2.4.1 Aerocapture Requirements

To further prepare for the aerocapture maneuver at Uranus and Neptune, the Aerocapture Mission Analysis Tool (AMAT) [22] was used to propagate aerocapture maneuvers using each

recorded vehicle. The feasibility of an aerocapture maneuver is defined by the theoretical corridor width (TCW), representing the range of entry flight path angles.

For the present study, TCWs of both 1°and 2°were considered based on past Ice Giant aerocapture study requirements [23].

For the propagated aerocapture maneuver, target capture orbit apoapsis radii of 1553575 km and 1491329 km for Neptune and Uranus, respectively, were arbitrarily considered following the AMAT baseline aerocapture examples [22]. The results of the AMAT aerocapture propagation for the range of optimally-shaped vehicles and their respective L/D ratios is shown in Figure 2.1.

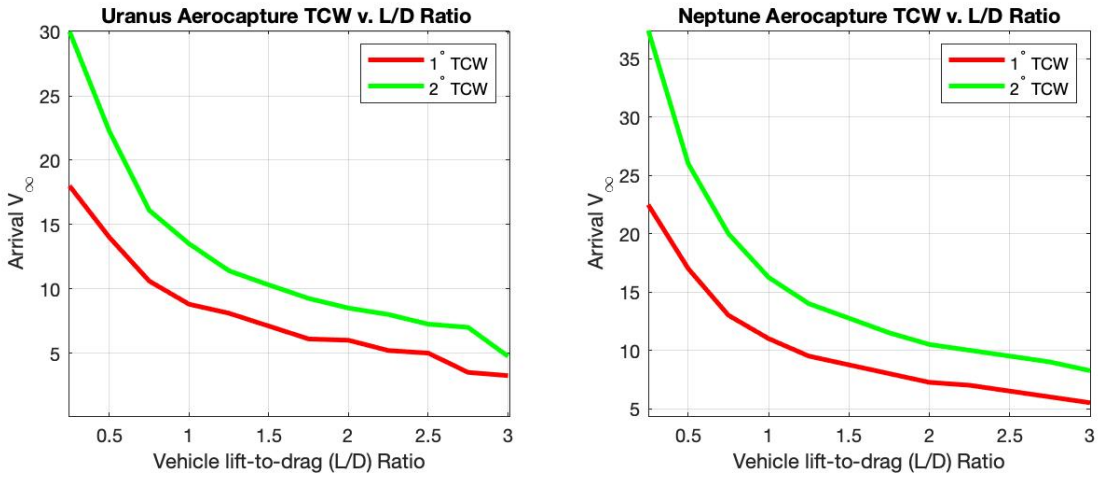

Figure 2.1: Ice Giant Aerocapture TCW v. L/D for Optimally Shaped Vehicles

For the heritage vehicles, there are slight variations in the TCW arrival V_∞ requirements due to varying shapes and ballistic coefficients. However, the heritage vehicle TCW requirements follow the same patterns estimated by the optimally-shaped 0.25-L/D vehicle in Figure 2.1.

The unique V_∞^- corresponding to the 1° and 2° TCWs will be used as lower bounds for the arrival velocity constraint in the trajectory optimization process. This ensures that the optimal trajectory for the chosen vehicle will allow for a sufficiently large aerocapture TCW at the given Ice Giant planet.

2.4.2 AGA Performance

To investigate the initial performance of the heritage and optimally-shaped vehicles in an AGA maneuver, a study has been conducted across all vehicles for a theoretical AGA maneuver. The input parameters of the vehicle study AGA maneuver are outlined below.

Table 2.2: AGA Simulation Variables for initial Vehicle Study

Planet	$V_p\ (km/s)$	$\beta_{s_i}\ (^\circ)$	$\phi\ (^\circ)$	$\theta_{atm}\ (^\circ)$	$V_{s_i}\ (km/s)$	$V_i\ (km/s)$
Venus	35.26	15.02	135.44	70.83	39.92	14.74

The given turn angle, ϕ, is well beyond the capabilities of a gravity-assist maneuver at Venus. Using the relationship between the spacecraft V_∞, ϕ, and the radius of closest approach, r_p, a GA with the previously defined parameters would have an r_p of 1207 km. As the mean radius of Venus is 6050 km, the turn angle ϕ of the AGA is well beyond the capabilities of a GA maneuver. For the given V_∞, the ϕ limit for a GA is approximately 90°.

2.4.2.1 Heritage Vehicles

The heritage vehicles considered in the current study include the Apollo CSM, Viking 1, Fire 2, PAET, Pioneer, Galileo, OSIRIS-REx, Pathfinder, Huygens, Stardust, Opportunity, and Beagle 2. Further vehicles were considered, but the previously-stated vehicles were chosen to represent the vehicle set for graphing purposes.

All heritage vehicle exhibited a trajectory that did not cruise at the reference altitude for the majority of the atmospheric flight, unlike typical AGAs. The higher L/D vehicles, such as the Apollo vehicle, stayed at the lowest altitude for a longer period of time, as shown in Figure 2.3a. This is likely due to the rapid planetocentric velocity decrease due to atmospheric drag, which is

much more dramatic on low-L/D vehicles.

The heating rates during atmospheric flight, shown in Figure 2.3b, show a much lower heating rate when compared to the optimally-shaped vehicles presented later in the study. While the lower heating rates seem promising, the planetocentric velocity, shown in Figure 2.2, shows a critical decrease in spacecraft velocity over the atmospheric flight.

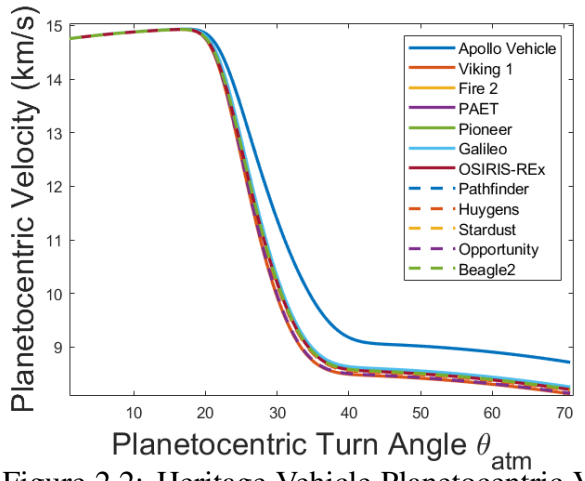

Figure 2.2: Heritage Vehicle Planetocentric Velocity during Venus AGA Study

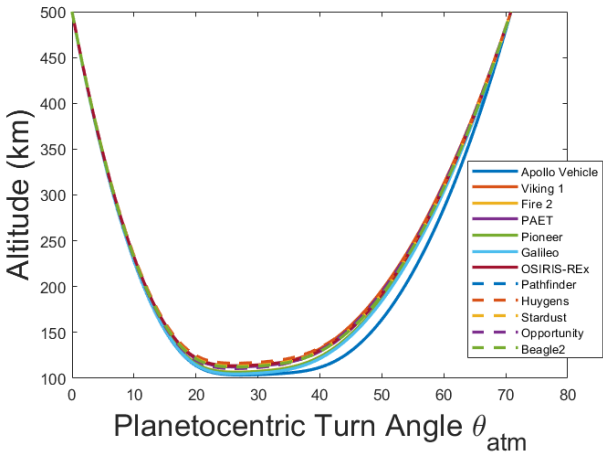

(a) Altitude v. Atmospheric Turn Angle

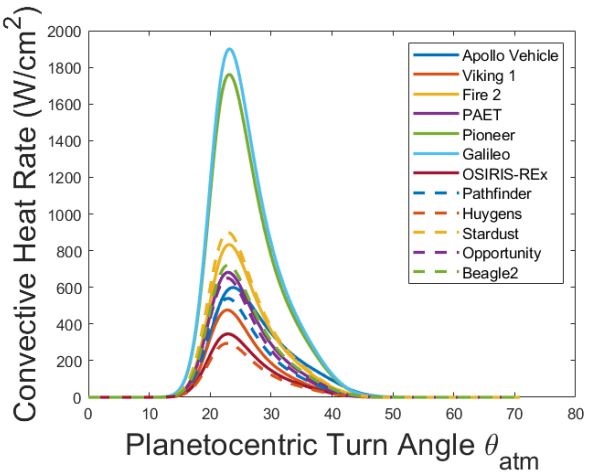

(b) Convective Heating v. Atmospheric Turn Angle

Figure 2.3: Venus AGA Heritage Vehicle Study Results

The velocity loss is so large that none of the heritage vehicles successfully reach Venus escape velocity upon atmospheric exit. This trend is repeated in further testing with different AGA planets and initial spacecraft velocities.

2.4.2.2 Optimally-Shaped Vehicles

The optimally-shaped vehicles represent theoretical waveriders with lower-L/D than previous studies. The vehicle with the largest L/D ratio is the Henning, et al [11] vehicle with a L/D of 3. The other optimally-shaped vehicles exhibit the same mass-to-area ratio as the Henning, et al [11] vehicle, with a reduction in L/D ratio. In addition, for comparison purposes, the highest performing heritage vehicle, Apollo, is graphed alongside the optimally-shaped vehicles.

All of the optimally-shaped vehicles exhibited an expected AGA altitude variance, shown in Figure 2.4a, with a majority of the atmospheric flight spent at the minimum altitude. There was slight variation in time spent at the lowest altitude, with the higher-L/D vehicles spending longer time compared to the lower-L/D vehicles.

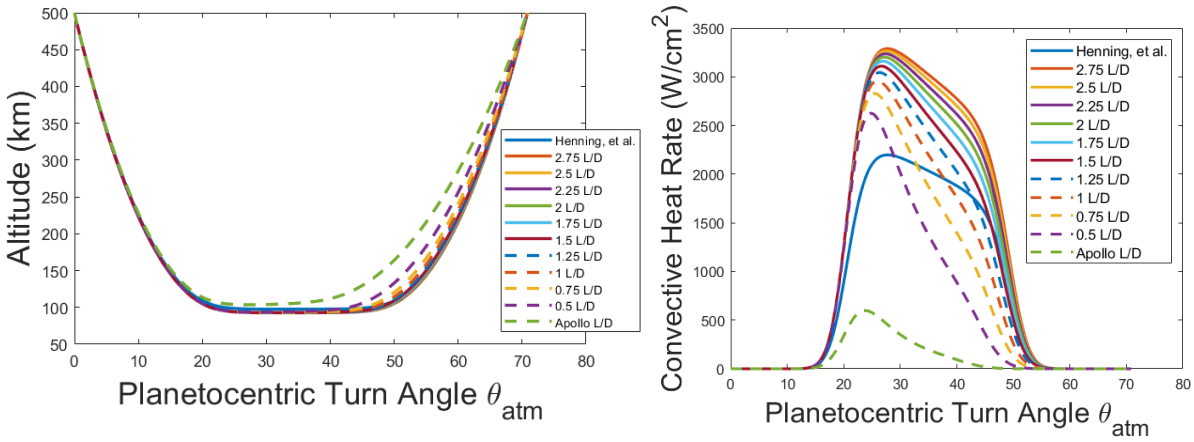

(a) Altitude v. Atmospheric Turn Angle (b) Convective Heating v. Atmospheric Turn Angle

Figure 2.4: Venus AGA Optimally-Shaped Vehicle Study Results

The convective heating rate over the atmospheric flight, shown in Figure 2.4b, is much larger than the heritage vehicle counterparts. This is very evident, as the Apollo vehicle received the largest convective heating rate among the heritage vehicles. In the optimally-shaped vehicle study, the Apollo vehicle is an order of magnitude smaller than all other vehicles.

Although the heating rates of the optimally-shaped vehicles are much higher, the velocity decrease due to atmospheric drag was smaller, as shown in Figure 2.5. As expected, the higher-L/D vehicles performed the AGA maneuver very efficiently, with minimal velocity loss due to drag. Although the mid-L/D vehicles did not retain velocity as well as the higher-L/D vehicles, they still performed much better than the heritage vehicles.

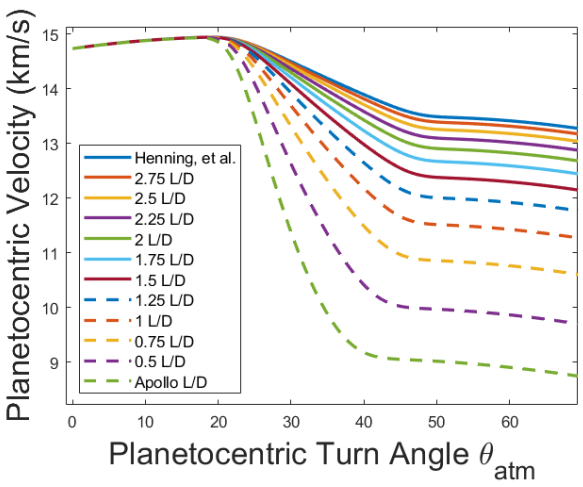

Figure 2.5: Optimally-Shaped Vehicle Planetocentric Velocity during Venus AGA Study

The ultimate ΔV after the AGA maneuver is shown in Figure 2.6. In the heritage and interplanetary vehicle study, only vehicles with a L/D ratio equal to or greater than 0.75 reached Venus escape velocity after the maneuver. With this in mind, only these vehicles are displayed.

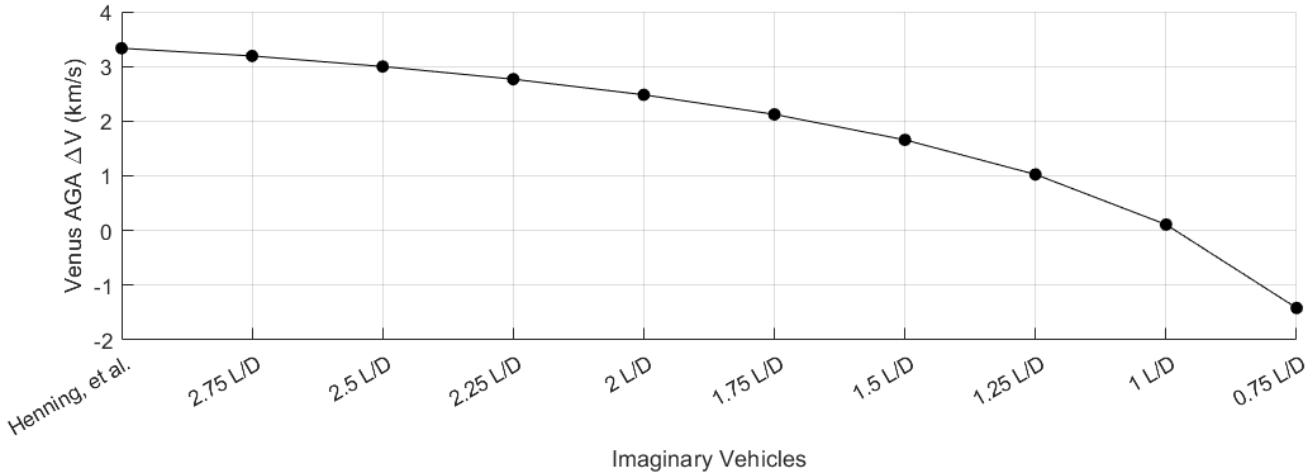

Figure 2.6: Optimally-Shaped Vehicle Venus AGA Study ΔV

For comparison, a GA performed at the edge of the Venusian atmosphere with the same V_∞ would result in a ΔV of 6.2928 km/s. Although this is beyond the performance of the heritage

vehicles shown in Figure 2.6, the GA has a turn angle ϕ of 90°, while the AGA reaches a ϕ of 135.44 °, thus allowing for further flexibility in planetary geometry requirements. This flexibility could potentially allow for additional launch windows and less reliance on gas giant GAs for outer-planetary missions.

2.5 Code Validation

The two-layer optimization approach is validated separately for each layer. The inner layer TPBVP successfully reproduces the AGA results presented by Henning, et al. [11], as well as the convective heating rate results presented by Lohar, et al. [12], as expected from the equation derivation process. The outer layer surrogate optimizer can be validated through examination of the optimization process. An example of the surrogate optimizer is shown in Figure 2.7 for a vehicle with a L/D of 2. The search parameters are for a January 2040 Uranus Arrival with a 1° TCW aerocapture requirement. In addition, the interplanetary trajectory is constrained to use only one AGA.

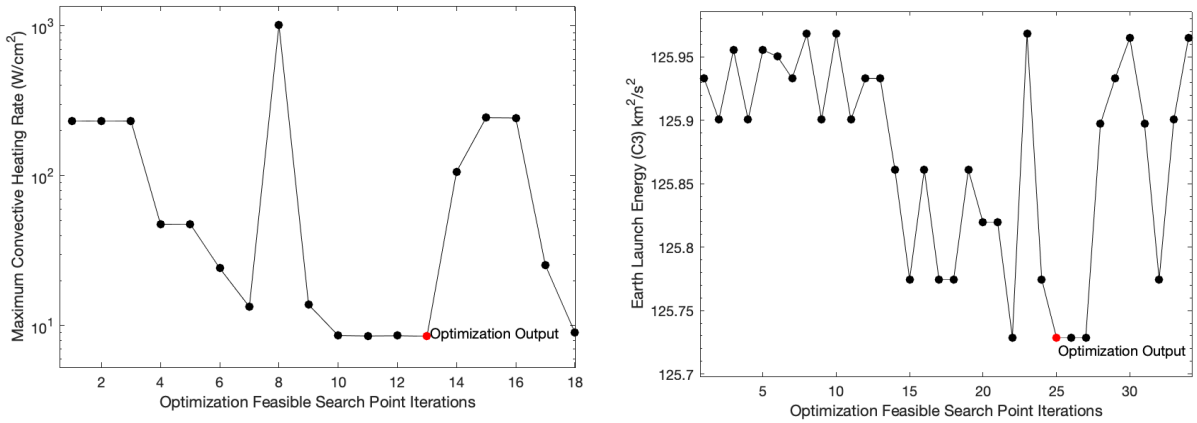

Figure 2.7: Validation of Surrogate Optimizer for Minimizing Convective Heating Rates (a) and minimizing Earth Launch $C3$ (b)

Only feasible trajectories identified through the optimization process are plotted in Figure

2.7, with the global minimum solution output by the optimizer designated by a red marker. Due to the nature of the surrogate optimizer and the non-continuous objective function, the optimization has a stopping criterion of 250 function evaluations over a one-month search period.

In both $C3$ and $q_{c_{max}}$ objective function variable options, the surrogate optimizer outputs the global minimum value and corresponding trajectory over the trajectory tradespace.

Chapter 3: Results

To begin the optimization process, an initial search of arrival dates was conducted for trajectories with one AGA (1-AGA) over the years of 2040 to 2060 using a vehicle with a lift-to-drag ratio of 2 (2-L/D). The 1-AGA trajectory option was chosen to begin the search as it was the most restrictive AGA option due to planetary geometry. The 2-L/D vehicle was chosen due to its mid-L/D relative to the study's set of vehicles. For the initial optimization search, the maximum convective heating rate during AGA was chosen as the objective function output to minimize.

The initial search led to the year 2040 being identified as the optimal year for arrival opportunities for both 1-AGA and 2-AGA Uranus missions.

For Neptune, there were no 1-AGA arrival opportunities within the 1° or 2° TCW V_∞^- requirements during the 2040-2060 search period. A 2-AGA trajectory search identified the year 2045 as an optimal arrival period.

For each planet, 3- and 4-AGA trajectory options were considered, but the current study setup favored the 1- and 2-AGA options. This is due to the nature of the TPBVP solution: As each AGA is solved for the largest final heliocentric velocity, the addition of more than 2 AGAs in a single trajectory results in one or more AGAs experiencing excessive convective heating. As there is no simple way to constrain the performance of an AGA in the current setup, the additional AGAs tend to have only small heliocentric velocity increases and large convective heating rates.

Due to this trend, only 1- and 2-AGA options are considered in the present study.

The results of the 1° and 2° TCW 2-AGA trajectory study for a 2-L/D vehicle is shown in Figure 3.1. For Uranus, each month of the year 2040 was processed through the two-layer optimization program to find the trajectory with a minimum convective heating rate. The optimization was performed with for both 1° and 2° TCW requirement constraints. For Neptune, the same approach was conducted with each month of the year 2045.

Specific optimal trajectories identified by the study are outlined in Appendix A.

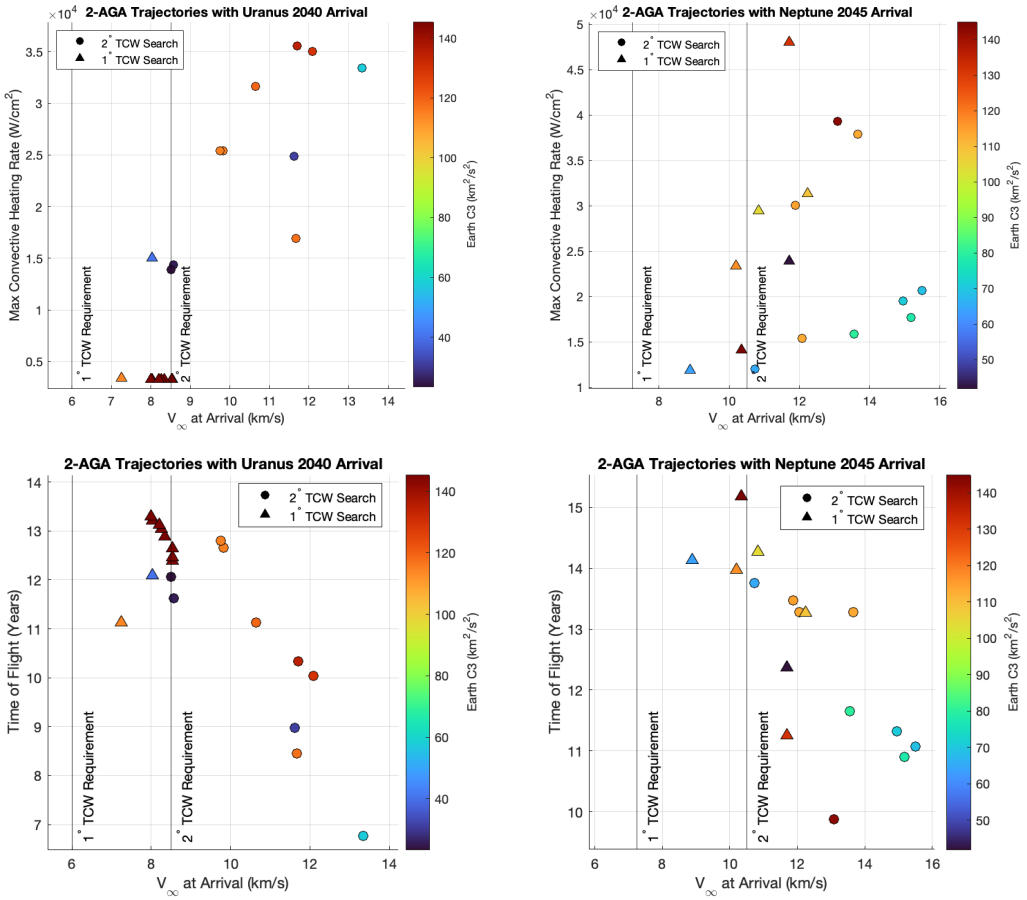

Figure 3.1: Maximum Convective Heating Rate (top) and TOF (bottom) of Optimal 2-AGA Trajectories for Uranus 2040 Monthly Arrivals and Neptune 2045 Monthly Arrivals, considering 1° and 2° aerocapture TCWs

3.1 Uranus

3.1.1 1-AGA Trajectories

A family of 1-AGA maneuvers with the 2-L/D vehicle allowed for distinct trajectories with arrivals 6 months of the year 2040 for a 2° TCW, and for all months of 2040 for a 1° TCW. In addition, every AGA was below a maximum convective heat rate of 300 W/cm^2. The trajectory family identified utilizes a high-altitude Earth AGA, which allows for maximum convective heating rates as low as 7 W/cm^2 during the AGA.

An example of the EEU trajectory family with a 2-L/D vehicle is shown in Figure 3.2. For this trajectory, the AGA allows for a heliocentric ΔV of 6.49 km/s alongside a large turn angle. The Uranus arrival V_∞^- is 8.509 km/s, within the 2° TCW requirements for the 2-L/D vehicle.

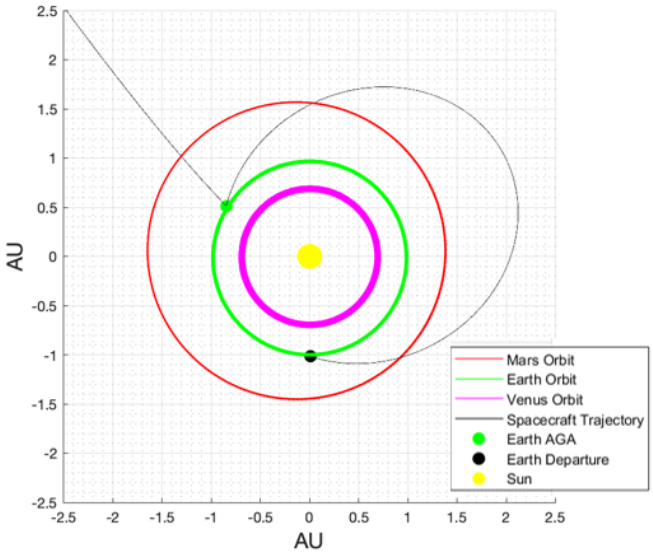

Figure 3.2: **Inner-Solar System Earth-Earth-Uranus AGA Trajectory for a 2-L/D vehicle**
Launch Date: 6/7/2029
Arrival Date: 8/16/2040

The high-altitude AGA is almost a hybrid of the GA and AGA maneuver, as the vehicle executes an atmospheric flight, shown in Figure 3.3, but does not display the expected characteristics of an AGA. In contrast to previous AGA studies, the high-altitude AGA does not spend a majority of the flight time at the reference altitude, and the atmospheric turn angle is moderate. Although these are not the op-

timal AGAs previously studied in literature, these high-altitude Earth AGAs allow for a higher launch frequency and a lower AGA vehicle L/D requirement.

The most attractive feature of the Earth-Earth-Uranus (EEU) trajectory family is the increase in launch opportunities; further optimizing for yearly arrivals from 2040 to 2055 leads to opportunities each year that are within the aerocapture constraints, with the exception of the year 2054. The periodic trajectories rendezvous with Earth 1 year, 7 months, and 26 to 28 days after the initial launch to perform the AGA. For each trajectory, the arrival V_∞ at Uranus varies from 8 - 8.5 km/s, which is just under the 2° TCW requirement for the 2-L/D vehicle. Further arrival dates past 2055 can be considered if the TCW requirement is relaxed to 1°. For each trajectory, the time of flight from Earth to Uranus ranged from 10 to 11 years.

In comparison, a previous study of GA trajectories to Uranus over a 50-year launch period identified only 10 distinct, feasible launches with V_∞^- of 8 km/s or larger [24]. If the previously discussed AGA EEU trajectory is utilized, there exist at least 15 distinct, periodic launch opportunities over just a 16-year period of study.

It is worth noting that the family of trajectories can be executed using heritage vehicles due to the nature of the high-altitude AGA. However, the heritage vehicles' arrival V_∞ is below the vehicle's 1° TCW requirement when utilizing this family of trajectories. Although the AGA EEU trajectory could potentially set up for propulsive capture about Uranus using heritage vehicles, it is unlikely to set up for a successful aerocapture maneuver.

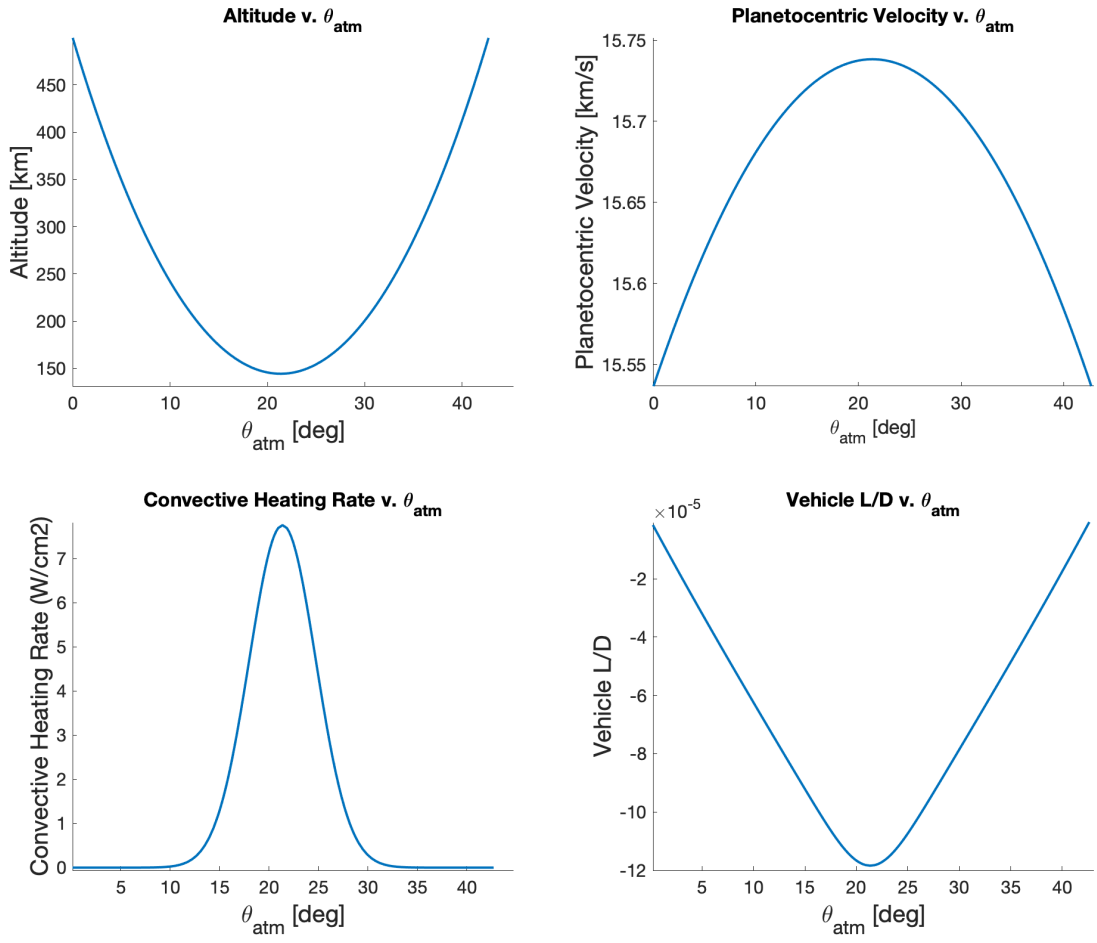

Figure 3.3: High-Altitude Earth AGA Characteristics for Earth-Earth-Uranus Trajectory with a 2-L/D vehicle

3.1.2 2-AGA Trajectories

The 2-AGA search for minimum convective heating rate allowed for distinct arrival opportunities in 11 months of 2040, for both 1° and 2° TCWs. The minimum convective heating rate for the 2° TCW arrival opportunities was 13908 W/cm^2, which exceeds the 8000 W/cm^2 upper limit of the NASA Heatshield for Extreme Entry Environment Technology (HEEET) [25]. If the arrival TCW is relaxed to 1°, the minimum convective heating rate for the 2040 arrival is 3256 W/cm^2, well within the HEEET technology limits.

An example of a 2-AGA, Earth-Earth-Earth-Uranus trajectory is shown in Figure 3.4. The first Earth AGA has a minimal ΔV increase of 0.5 km/s, but the maneuver serves to align the trajectory for a subsequent high-altitude Earth AGA with a ΔV of 6.44 km/s. This trend is repeated throughout the 2-AGA trajectory study, with the first AGA having minimal ΔV while setting up for a high-performing second AGA.

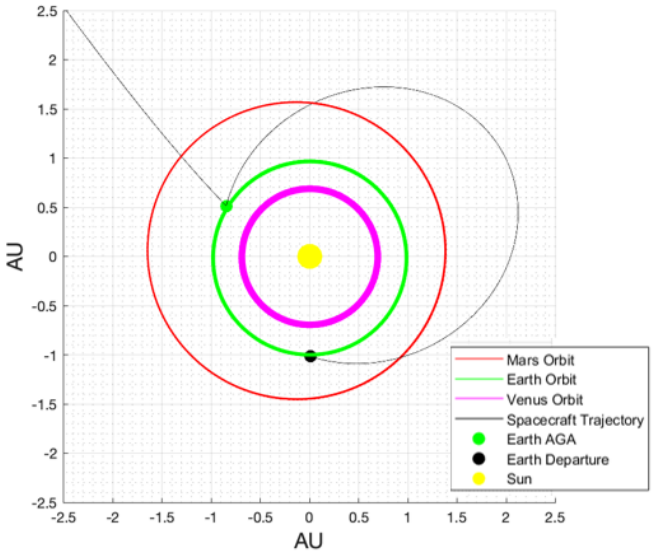

Figure 3.4: **Inner-Solar System Earth-Earth-Earth-Uranus AGA Trajectory for a 2-L/D vehicle**
Launch Date: 11/1/2027
Arrival Date: 12/17/2040

As the second AGA characteristics are very similar to the previous Figure 3.3, only the first AGA characteristics are displayed in Figure 3.5, for brevity.

The 2° TCW opportunities use an equal mixture of Earth, Venus, and Mars combinations in its trajectory solutions. The 1° TCW opportunities, however, tend to use only Earth and Venus combinations, with only two Mars AGAs over the 11 trajectories.

A summary of the optimal 1- and 2-AGA Uranus aerocapture trajectories over the year 2040 is shown in Table 3.1.

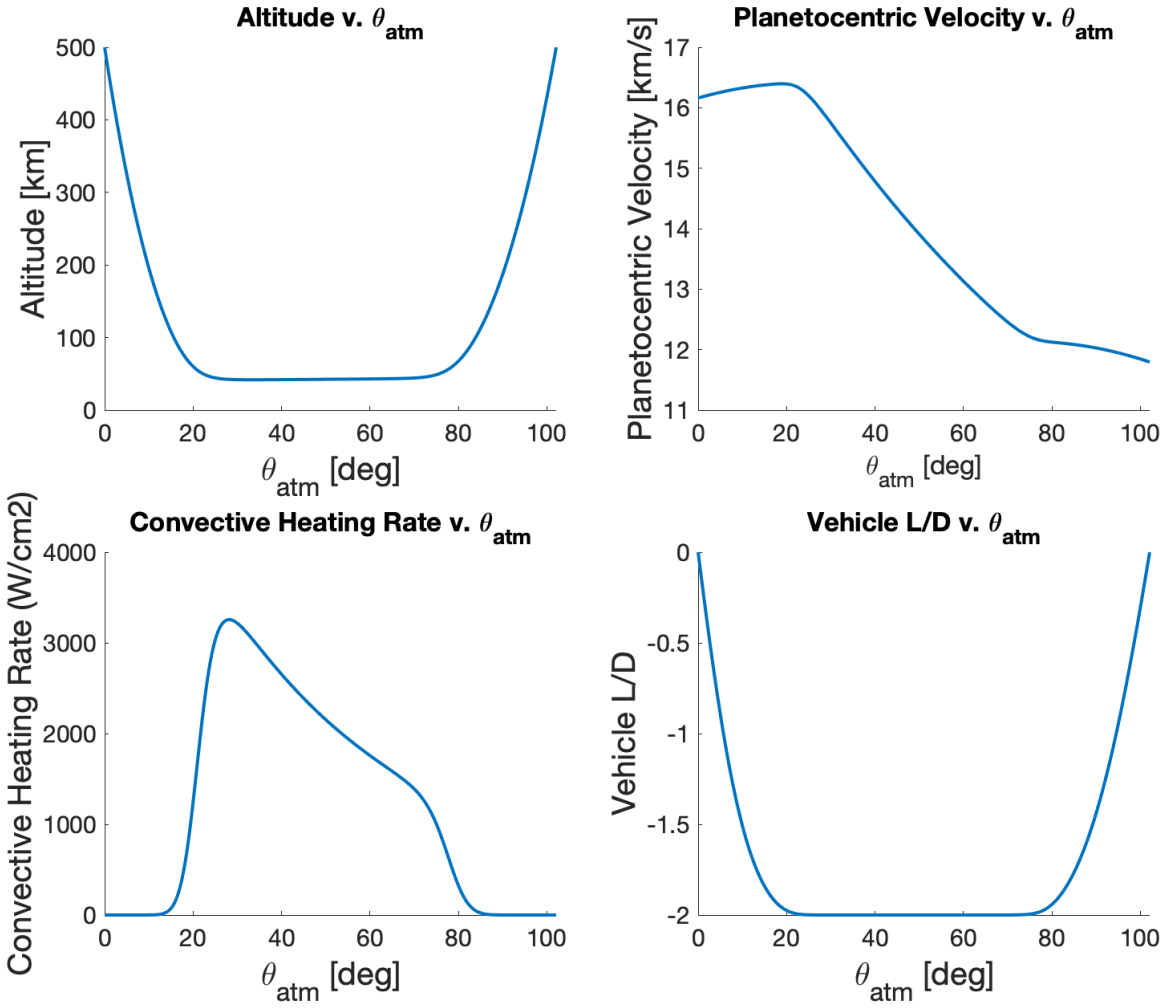

Figure 3.5: First Earth AGA Characteristics for Earth-Earth-Earth-Uranus Trajectory with a 2-L/D vehicle

Table 3.1: **2040 Uranus Optimal Arrival Windows with minimum convective heating rates**

Number of AGAs	**TCW ° Requirement**	**Month**	$q_{c_{max}}\ W/cm^2$
1	2	August 2040	7.76
1	1	February 2040	5.93
2	2	June 2040	13908
2	1	December 2040	3256

3.2 Neptune

3.2.1 2-AGA Trajectories

The 2-AGA search for Neptune allowed for distinct arrival opportunities during 11 months of 2045 for the 2° TCW requirement, and for 10 months of 2045 for the 1° TCW requirement.

An example of a 2-L/D Earth-Venus-Mars-Neptune (EVMN) trajectory is shown in Figure 3.6, with the Venus and Mars AGA characteristics outlined in Figures 3.7 and 3.8. The Venus AGA allows for a moderate ΔV increase of 5.98 km/s while also setting up for a large atmospheric turn angle at Mars that results in a ΔV increase of 18.41 km/s. The Martian atmospheric flight leads to an extreme maximum convective heating rate greater than 35000 W/cm^2. Although this rate is beyond the limits of the NASA HEEET, if the heating were to be addressed through alternate atmospheric trajectories, the trajectory would be attractive due to the high-performing maneuvers and planetary geometry options.

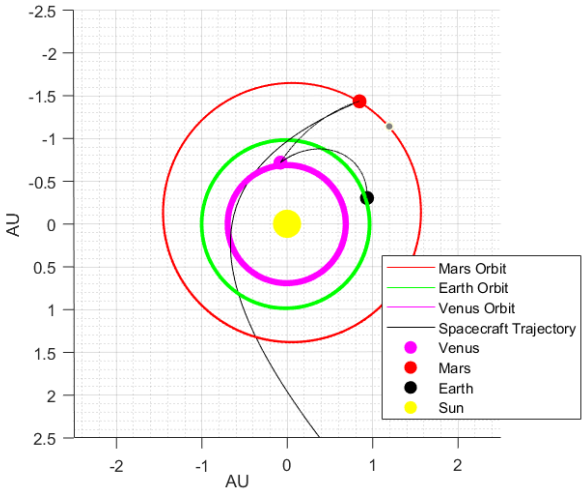

Figure 3.6: **Inner-Solar System Earth-Venus-Mars-Neptune AGA Trajectory for a 2-L/D vehicle**
Launch Date: 1/9/2036
Arrival Date: 11/23/2045

For the 2° TCW results, the minimum convective heating rate over the 11 trajectories was 11979 W/cm^2. The 1° TCW results had a minimum convective heating rate over the 11 trajectories of 11854 W/cm^2. In contrast to the Uranus trajectory search, the 1° TCW Neptune trajectory

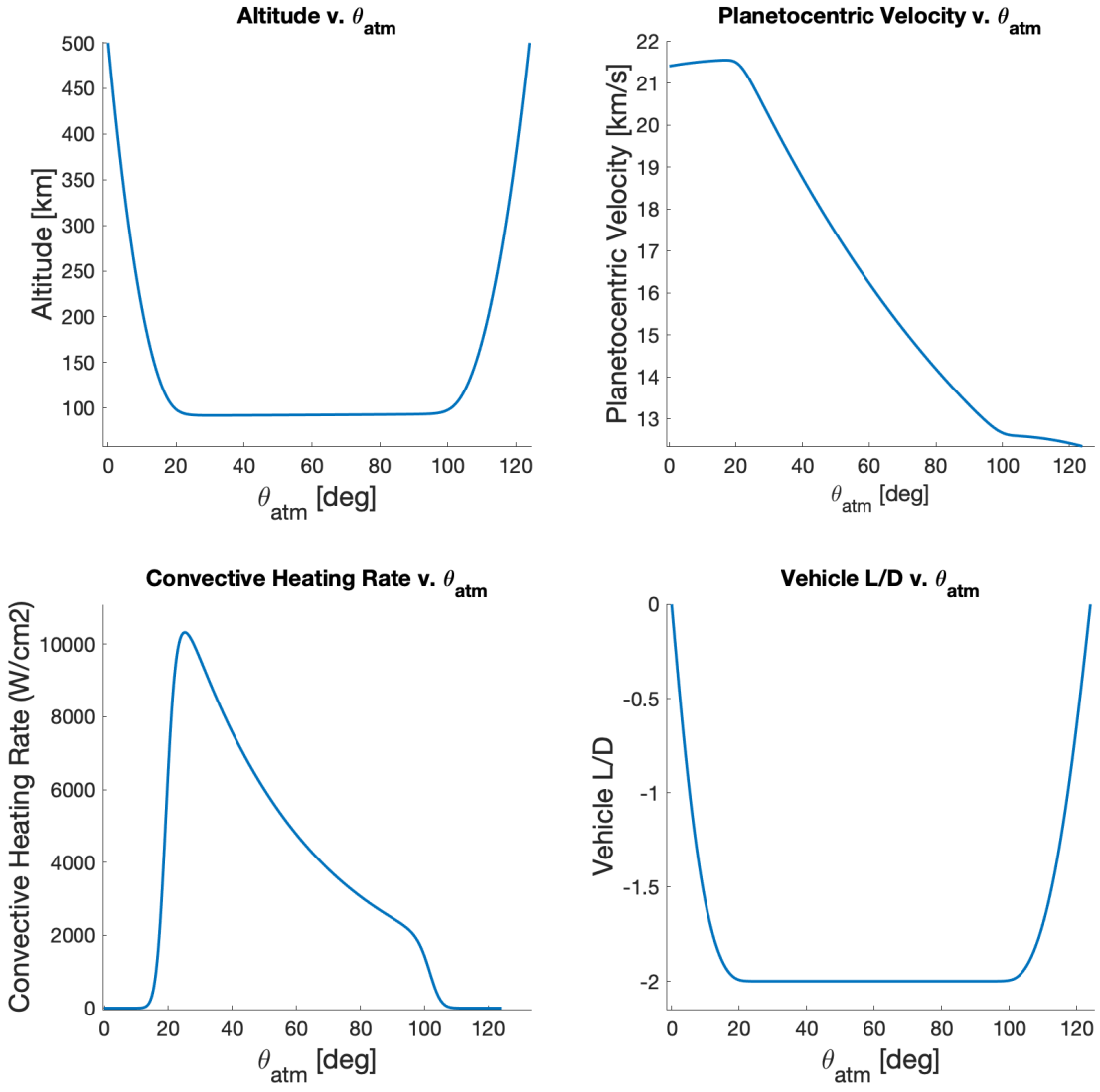

Figure 3.7: Venus AGA Characteristics for Earth-Venus-Mars-Neptune Trajectory with a 2-L/D vehicle

options did not see a large reduction in minimum convective heating rate when compared to the 2° TCW. This was due to the high V_∞^- values found in the 1° TCW optimization results, despite the smaller V_∞^- constraint. This was a pattern that emerged in both Uranus and Neptune studies, due to the derivation of the AGA TPBVP for maximum heliocentric velocity and the 5 km/s range used in the V_∞^- constraints. However, the Neptune 1° TCW V_∞^- optimal results were much closer

to the 2° TCW V_∞^- requirements when compared to the Uranus optimal result counterparts, likely due to the larger V_∞^- constraints for Neptune aerocapture. This pattern is demonstrated clearly in the overall optimization results of Figure 3.1, with many Neptune 1° TCW optimal trajectories surpassing the 2° TCW requirement.

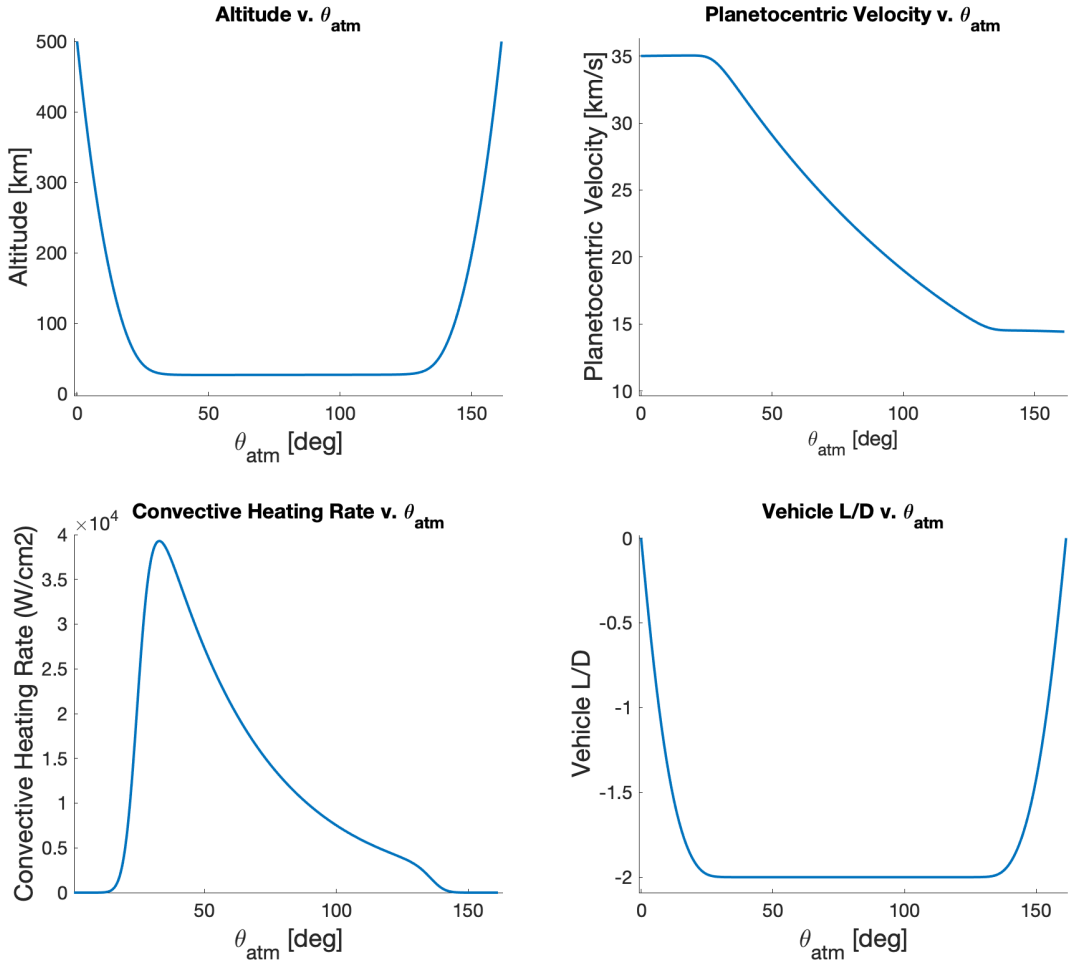

Figure 3.8: Mars AGA Characteristics for Earth-Venus-Mars-Neptune Trajectory with a 2-L/D vehicle

In addition, both 1° and 2° TCW trajectory solutions favored Venus and Mars AGA combinations, with seventeen out of twenty-two trajectory opportunities utilizing a Venus-Mars AGA. The 1° TCW opportunities featured more Earth AGAs, but a majority of the AGA combinations

were still primarily composed of Venus-Mars AGAs.

It is worth noting that the high heating rates for the 2-AGA trajectories are a shortcoming in the current AGA TPBVP setup. As the AGA TPBVP finds the optimal AGA for final heliocentric velocity, the last AGA computed often outperforms the first AGA. This leads the first AGA to perform a lower ΔV increase to set up for an interplanetary trajectory that ultimately decreases the spacecraft velocity to prepare for the high performance of the following AGA. As the program iterates backwards from the Ice Giant planet to the last AGA, the last AGA is the highest-performing AGA in the system. Further studies would require the optimizer to consider less-than-optimal AGAs, perhaps by rederiving the TPBVP to minimize the convective heat rate.

A summary of the 2-AGA Neptune aerocapture trajectories over the year 2045 is shown in Table 3.2.

Table 3.2: **2045 Neptune Optimal Arrival Windows with minimum convective heating rates**

Number of AGAs	**TCW $^\circ$ Requirement**	**Month**	$q_{c_{max}}\ W/cm^2$
2	2	January 2045	11979
2	1	June 2045	11854

3.3 AGA Vehicle Study

The previous Neptune and Uranus studies were performed with a 2-L/D vehicle to establish a baseline for the trajectory optimization dates. The study's minimum convective heating months, outlined in Tables 3.1 and 3.2, were then used as arrival date constraints for trajectory optimization across the vehicle set.

For the Uranus 1- and 2-AGA trajectories, the 1° TCW allowed for trajectories with lower-

L/D vehicles when compared to the 2° TCW solutions. For Neptune, however, the same vehicles were able to complete both the 1° and 2° TCW solutions.

The lowest L/D solution was found with a optimally-shaped 1.25-L/D vehicle in the 2° TCW 2-AGA Neptune, 1° TCW 2-AGA Uranus, and the 1° TCW 1-AGA Uranus cases. The 1.25-L/D vehicle for the 1° TCW, 2-AGA Uranus trajectory is shown in Figure 3.9. For brevity, as this trajectory closely follows the previously-studied 2-L/D vehicle EEEU trajectory, only the second Earth AGA characteristics are shown in Figure 3.10. The first Earth AGA has a minimal ΔV of 0.02 km/s, followed by a high-altitude Earth AGA with a ΔV of 6.43 km/s. The maximum convective heating rate during the Earth AGAs is 2888 W/cm^2, 368 W/cm^2 less than the 2-L/D vehicle performing a similar trajectory in Figure 3.9 and well within the NASA HEEET capabilities.

Across the vehicle testing set, the average lowest L/D solution was with a 1.5-L/D vehicle. Although this L/D requirement is beyond current interplanetary vehicle capabilities, it is still a reduction from previous literature requirements.

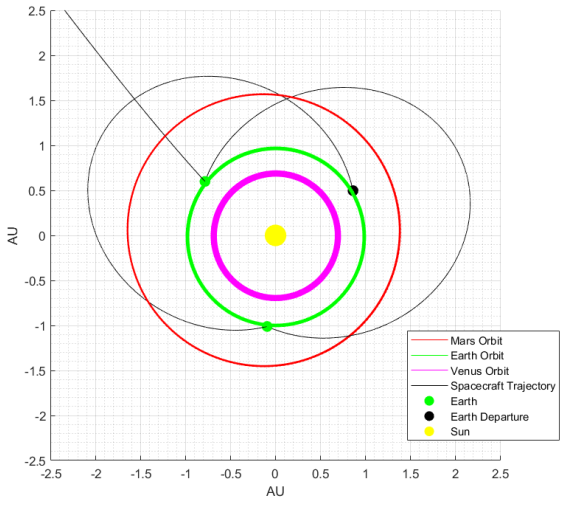

Figure 3.9: **Inner-Solar System Earth-Earth-Earth-Uranus trajectory for a 1.25-L/D Vehicle**
Launch Date: 10/26/2027
Arrival Date: 12/31/2040

No heritage interplanetary vehicle was able to complete the AGA trajectory while meeting the aerocapture arrival V_∞^- requirements. This is due to the larger arrival V_∞^- requirements for low-L/D vehicles. If this requirement is relaxed, heritage vehicles can complete certain high-altitude AGAs.

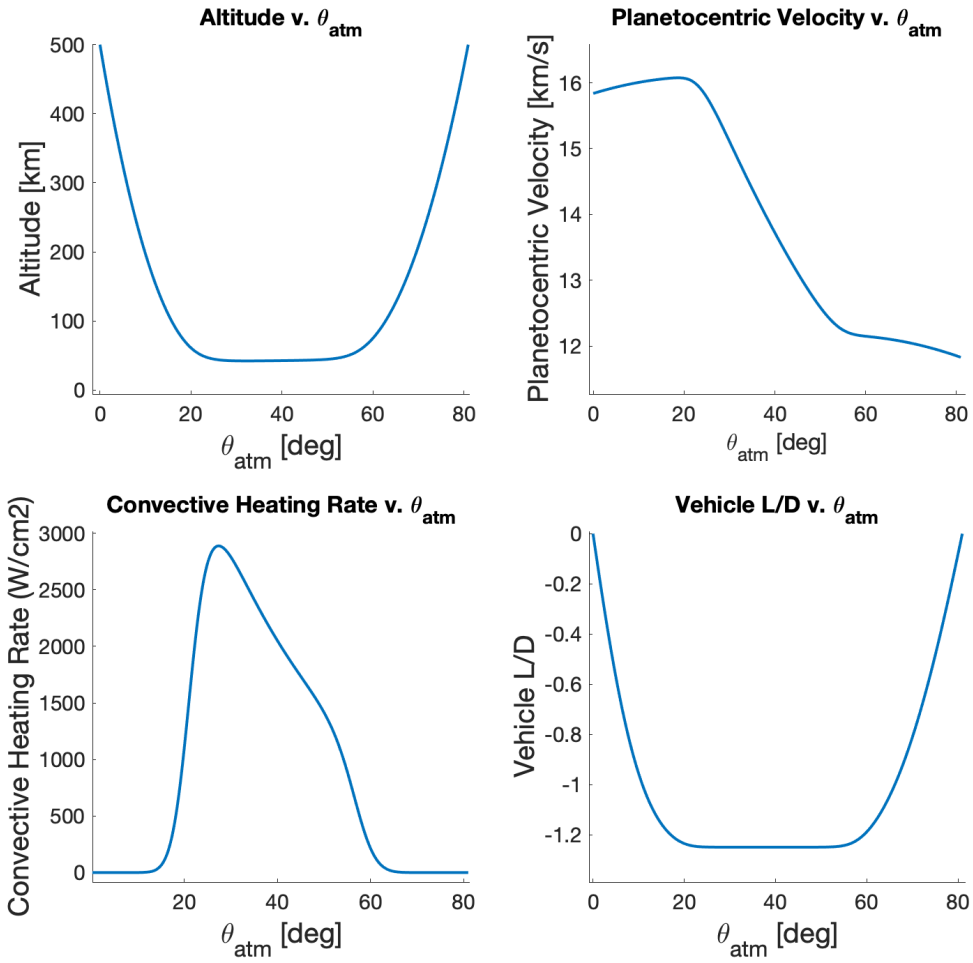

Figure 3.10: Second Earth AGA characteristics for an Earth-Earth-Earth-Uranus trajectory with a 1.25-L/D Vehicle

Both Mars AGAs for the EMMN trajectory display the characteristics of a typical AGA, with the majority of the flight time spend at the lowest altitude with the maximum L/D maintained. In addition, the vehicle flies at a bank angle of 180°, corresponding to an upside-down orientation, similar to results found in the higher-L/D vehicle AGAs of Lohar et al [12] and Henning et al [11].

The minimum convective heating rates were largely uncorrelated to the vehicle L/D. Although the lower-L/D vehicles experienced lower convective heating rates when compared to

the higher-L/D vehicles, the larger V_∞^- requirements enforced by the vehicle's TCW resulted in higher planetocentric velocities during the AGA. Due to the dependence on planetocentric velocity when calculating the convective heating rate, the overall heating rates across the vehicles were similar.

The overall lowest-L/D vehicles that successfully perform AGAs to set up for aerocapture are shown for each of the optimal months in Table 3.3.

Table 3.3: **Lowest-L/D Vehicles for AGA Trajectories with Aerocapture at Uranus and Neptune**

Vehicle L/D	**Ice Giant**	**AGAs**	**TOF (yrs)**	$C3$ $(\frac{km^2}{s^2})$	$q_{c_{max}}$ $(\frac{W}{cm^2})$	V_∞^- $(\frac{km}{s})$	**TCW (°)**
2	U	E	11.15	126.10	7.76	8.50	2
1.25	U	E	11.64	125.73	5.95	8.14	1
1.5	U	ME	11.29	116.76	36868	10.56	2
1.25	U	EE	13.19	134.58	2888	8.16	1
1.25	N	VM	11.58	44.67	34746	15.89	2
1.25	N	VM	12.34	53.61	33683	11.14	1

3.4 Minimum $q_{c_{max}}$ Optimization Trends

During the 2-AGA trajectory search for Uranus and Neptune, certain patterns arose with AGA combinations and maximum convective heating rates.

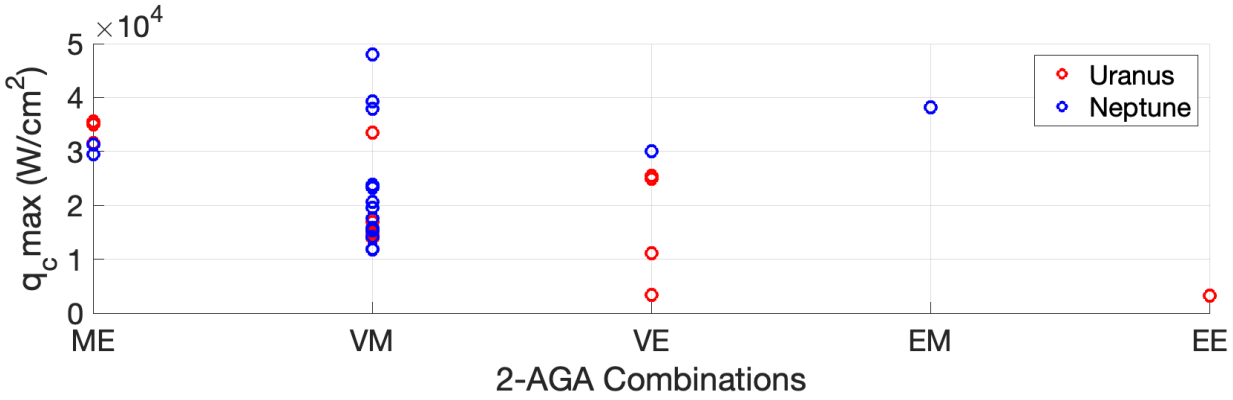

Figure 3.11: Optimal 2-L/D Vehicle 2-AGA Trajectory Combinations v. Convective Heating Rate

The Neptune trajectories consistently had a higher heating rate when compared to the Uranus trajectories, as expected from the larger V_∞ requirements. The majority of the optimization testing results were under 35000 W/cm^2. The most common combination by far was the Venus-Mars AGA, due to the geometry options. For the 2-L/D vehicle testing, the 2-AGAs consecutively at the same planet was not often the optimal solution, with the only solution being a singular Mars-Mars AGA combination. The current trend suggests that with a 2-L/D vehicle over the year 2040 for Uranus would have a more consistent heating rate during the Venus-Mars (VM) AGAs. In comparison, Neptune could use the VM AGAs, but a lower heating rate was also experienced during the Venus-Earth AGA combination.

Combinations of AGAs across the vehicle testing study can also be analyzed:

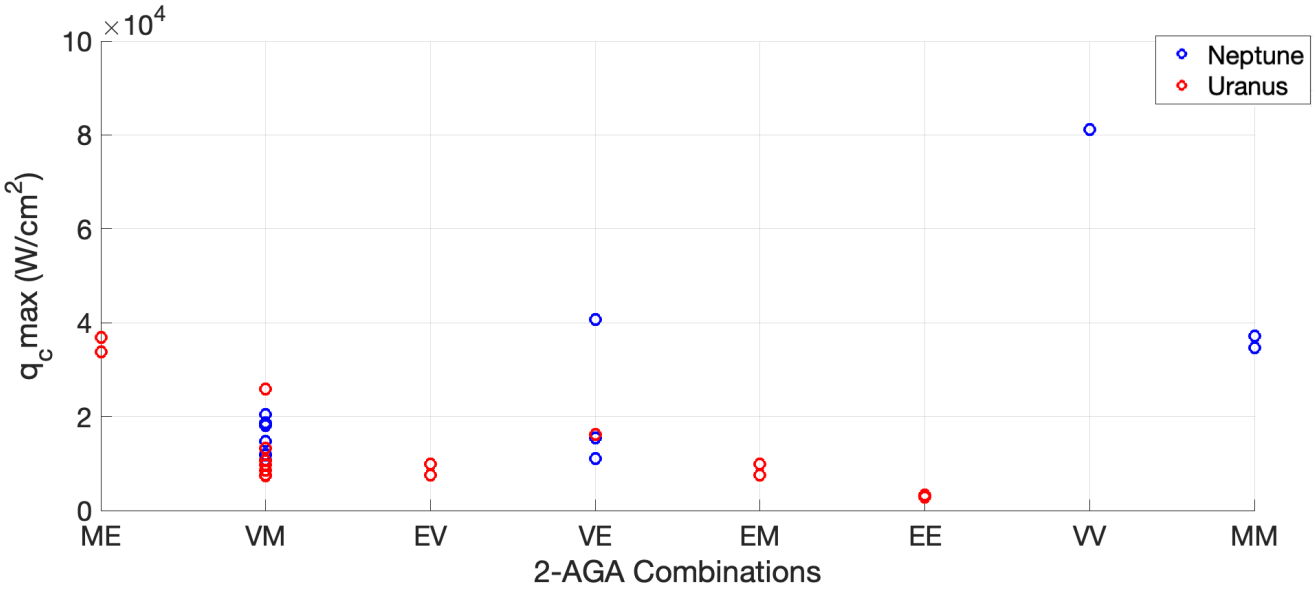

Figure 3.12: Optimal Vehicle Study Set 2-AGA Trajectory Combinations v. Maximum Convective Heating Rate

Compared to Figure 3.11, the vehicle testing study included a larger range of AGA combinations, with combinations of repeated AGA planets, which was not seen in Figure 3.11. The overall maximum heating rate results still showed a lower trend with Uranus trajectories over Neptune trajectories. A majority of the testing points were below the 20000 W/cm^2 mark, lower than the 2-L/D vehicle combinations average. The vehicle study did have outliers beyond the 2-L/D vehicle maximums, namely from the Neptune trajectory VV combination. Overall, the range of L/D-ratio vehicles tend to experience lower heating rates and larger AGA combination variety.

3.5 Minimum $C3$ Opportunities

The optimization approach can also be repeated with the $C3$ Earth launch energy as the objective function. In order to assess the usefulness of AGA trajectories with respect to $C3$

requirements, a comparison can be drawn from the 2030-2040s aerocapture trajectory search performed by Girija et al [23] and displayed in the NASA Aerocapture White Paper [3].

To perform the assessment, the 2-L/D vehicle trajectory is optimized for the lowest $C3$ over the years 2040 and 2045 for Uranus and Neptune, respectively.

In this case, the V_∞^- requirement for Uranus is set at 16.5 km/s and at 18 km/s for Neptune. These values were chosen specifically to sit at the upper limits of GA trajectories [3] but are also within the 2° TCW requirement for the 2-L/D vehicle.

In the 2030-2040s Girija et al search [23], there exist only 15 Neptune GA trajectory opportunities with a V_∞^- greater than 18 km/s and a $C3$ less than 50 km^2/s^2. For Uranus, there exist only 17 GA trajectory opportunities with a V_∞^- greater than 16.5 km/s and a $C3$ less than 30 km^2/s^2. To roughly assess the usefulness of AGA trajectories over GA counterparts for setting up aerocapture maneuvers, the study will use these values as guidelines for the optimization search.

The Neptune minimum $C3$ search identified 6 distinct arrival opportunities during the year 2045 alone that met the $V_\infty^- > 18$ km/s and $C3 < 50$ km^2/s^2 guidelines, in comparison to the 15 trajectory opportunities identified over the 20-year Girija et al. [23] search. In addition, each of the 15 Girij, et al. [23] trajectory opportunities relied on a Jupiter GA, which further constrains launch opportunities past 2050. The 2-AGA Neptune opportunities utilized different combinations of inner solar system AGAs, which could further increase the number of potential launch opportunities for following decades.

The Uranus minimum $C3$ search identified only 2 distinct arrival opportunities during the year 2040 that met the requirements, in comparison to the 17 trajectory opportunities from the 20-year Girija, et al. [23] search. As the GA opportunities also relied upon a Jupiter GA, the

Uranus inner-solar system AGA trajectories may allow for more frequent launches independent from gas giant positions, but further study over subsequent decades is required.

Chapter 4: Conclusions

An assessment of aerogravity-assisted trajectories for preparation of aerocapture at the Ice Giants has been conducted using a two-layer optimization approach. To address the lack of flight-tested, high-L/D interplanetary vehicles, the study also investigated the use of heritage, low-L/D vehicles alongside optimally-shaped vehicles with L/D lower than present literature.

Ultimately, heritage vehicles were not able to complete the optimal AGA trajectories while meeting the arrival V_∞^- set by aerocapture TCW requirements. This is due to the larger V_∞^- requirements for low-L/D vehicle aerocapture. Although the heritage vehicles could not properly set up for aerocapture, there exist certain high-altitude AGAs that could be completed if the V_∞^- requirement was reduced. The potential of high-altitude AGAs with heritage vehicles for propulsive capture at the Ice Giants is worth investigating.

The lowest-L/D vehicle to complete the optimal AGAs and set up for aerocapture was a 1.25-L/D optimally-shaped vehicle, which is still a large reduction in the L/D of past literature studies.

With a 2-L/D vehicle, a family of periodic trajectories using a high-altitude Earth AGA was identified for Uranus aerocapture opportunities. The family of trajectories was particularly appealing as it allowed for yearly arrival opportunities from 2040 - 2055, with the exception of 2054. Past 2055, the V_∞^- is below the 2° TCW aerocapture requirement, but the trajectory itself

could set up for 1° TCW aerocapture or even a propulsive orbital capture. This trajectory family could allow for periodic launches that are not reliant on Jupiter or Saturn GAs.

In addition, a comparison to past GA trajectories for Ice Giant aerocapture [23] showed that AGA trajectories may have more launch opportunities with low $C3$ and high arrival V_∞^-. As only one arrival year was studied for each Ice Giant, and the past GA study encompassed two decades, further investigation must be performed to validate the trends. From the initial studies, AGAs allow for 6 distinct trajectory opportunities with V_∞^- greater than 18 km/s and $C3$ less than 50 km^2/s^2 in the year 2045 alone for Neptune, whereas the previous GA study [23] found only 15 trajectory opportunities over the two decade period with the same requirements. The AGA opportunities also used a mixture of different 2-AGA combinations, whereas the GA trajectories relied on a Jupiter GA.

Ultimately, 1- and 2-AGA trajectories for aerocapture at Uranus have feasible options using current heatshield technologies and launch vehicle capabilities. To set up for aerocapture at Neptune, large convective heating rates would require thermal protection systems past current technology readiness levels. Further investigation on atmospheric guidance and control schemes for AGAs could reduce the heating rates, but would require in-depth study.

The increase in launch opportunities and reduction in the reliance on gas giant GAs is the main benefit of AGA trajectories for aerocapture at the Ice Giants. Additional studies are needed to thoroughly investigate the trajectory space across upcoming decades. However, the initial trajectory results suggest that AGA trajectories could surpass GA trajectories in preparing for Ice Giant aerocapture opportunities.

4.1 Future Work

As the largest deterrent from aeroassisted maneuvers is in the high heating rates on the vehicle, further study must be conducted to investigate possible methods of heat reduction. Future studies could discern the optimal AGA maneuver for minimum convective heating rate over the same range of dates considered in the present study. In addition, further investigation on AGA atmospheric guidance and control schemes could reduce the heating rates, but would require in-depth study. As the heat load on a vehicle causes ablation of the vehicle's shape, the L/D deterioration due to ablation would need to be considered in high-heating rate trajectories.

In addition, if the AGA TPBVP is rederived to optimize for the minimum convective heating rate instead of the maximum heliocentric velocity, further trajectory options could become available over the same time period as the present study. This would address the over-performance of certain AGAs in the present study's solution, and instead split the overall performance over multiple AGAs. This would in turn require investigation of 3+ AGA trajectories. In addition, the AGA TPBVP could be further defined by including three-dimensional equations of motion, allowing for further degrees of freedom for the spacecraft.

Future code work could include a higher-fidelity interplanetary trajectory simulation, alongside a patched conics method, to account for all realistic forces on the spacecraft. This would address the estimation approach of the current study, allowing for a more precise trajectory analysis.

In addition, the use of a higher computing machine would allow for further trajectory analysis. As the present study dataset was limited due to computation power and time, a more thorough study over the 2040-2060 arrival years, along with subsequent decades, would allow for a much

more thorough assessment of inner solar system AGAs for aerocapture at the Ice Giants. In addition, the high-V_∞^- study must be replicated over the years following 2040, for Uranus, and 2045, for Neptune, to ensure the trend of high-V_∞^- alongside low-$C3$s.

A more in-depth study on aerocapture must be conducted to truly assess aerocapture options from AGA trajectories. Aerocapture maneuvers of varying post-maneuver apoapsis could be investigated to further define the trajectory space, which may allow for further mission trajectory opportunities.

Appendix A: Ice Giant AGA Trajectory Catalog

The following catalog represents the 2-L/D, optimally shaped vehicle trajectory searches that were performed for the years 2040 for Uranus and 2045 for Neptune. All trajectories represent distinct launch and arrival dates. Alternate trajectories that fall within 2 months of the distinct launches are omitted for brevity.

A.1 Uranus 2040 Search

A.1.1 $C3 < 150\ km^2/s^2$ and Convective Heating Rates $< 8000\ W/cm^2$

Ice Giant	**AGAs**	**Earth Dep. Date**	**TOF (years)**	$C3\ (\frac{km^2}{s^2})$	$q_{c_{max}}\ (\frac{W}{cm^2})$	**Arrival** $V_\infty(\frac{km}{s})$	**TCW** (°)
U	E	6/7/2029	11.15	126.10	7.76	8.5	2
U	EE	10/30/2027	12.39	144.91	3261	8.539	2
U	EE	10/17/2026	13.21	145.42	3258	8.03	1
U	E	6/24/2028	11.64	125.73	5.92	8.16	1
U	VE	3/17/2029	11.12	113.57	3390	7.25	1

A.1.2 $C3 < 150\ km^2/s^2$ and Convective Heating Rates $> 8000\ W/cm^2$

Ice Giant	**AGAs**	**Earth Dep. Date**	**TOF (years)**	$C3\ (\frac{km^2}{s^2})$	$q_{c_{max}}\ (\frac{W}{cm^2})$	**Arrival** $V_\infty(\frac{km}{s})$	**TCW** (°)
U	VE	7/26/2027	12.79	114.51	25422	9.75	2
U	VM	5/22/2028	11.62	25.76	14375	8.56	2
U	VM	6/7/2028	12.66	114.51	13908	9.82	2
U	ME	3/12/2029	11.13	119.25	31629	10.64	2
U	ME	3/12/2029	11.13	119.25	31629	10.64	2
U	ME	8/9/2030	10.04	129.71	35012	12.09	2
U	VE	7/6/2031	8.97	31.38	24864	9.82	2
U	VE	4/11/2032	8.45	117.20	16902	11.66	2
U	VM	5/11/2033	6.773	57.77	33445	13.34	2

A.2 Uranus EEU Trajectory Family

Ice Giant	**AGAs**	**Earth Dep. Date**	**TOF (years)**	$C3$ ($\frac{km^2}{s^2}$)	$q_{c_{max}}$ ($\frac{W}{cm^2}$)	**Arrival** $V_\infty(\frac{km}{s})$	**TCW** (°)
U	E	6/17/2030	10.81	125.87	19.79	8.52	2
U	E	7/1/2031	11.06	125.99	5.90	8.54	2
U	E	6/13/2028	11.64	125.72	5.93	8.16	1
U	E	6/27/2032	11.33	125.66	6.82	8.19	1
U	E	7/8/2033	11.35	125.933	12.19	8.29	1
U	E	7/6/2034	11.18	125.54	6.92	8.22	1
U	E	7/29/2035	11.26	125.82	20.37	8.26	1
U	E	7/23/2036	11.32	125.43	5.98	8.30	1
U	E	7/21/2037	10.92	125.83	92.55	8.39	1
U	E	7/26/2038	11.24	125.25	7.78	8.19	1
U	E	8/3/2039	11.35	125.61	9.91	8.19	1
U	E	7/31/2039	11.51	125.74	156.33	8.03	1
U	E	8/2/2040	11.54	125.51	18.52	7.98	1
U	E	8/11/2041	11.43	125.51	16.18	8.09	1
U	E	4/18/2044	11.59	126.05	7.14	6.16	1

A.3 Neptune 2045 Search

A.3.1 $C3 < 150\ km^2/s^2$ and Convective Heating Rates $> 8000\ W/cm^2$

Ice Giant	**AGAs**	**Earth Dep. Date**	**TOF (years)**	$C3\ (\frac{km^2}{s^2})$	$q_{c_{max}}\ (\frac{W}{cm^2})$	**Arrival** $V_\infty(\frac{km}{s})$	**TCW** (°)
N	VM	4/22/2031	13.76	64.93	11979	10.74	2
N	VM	4/10/2032	13.28	113.59	37881	13.66	2
N	VE	4/18/2032	13.47	114.50	30031	11.88	2
N	VM	2/26/2033	12.15	41.97	23593	12.15	2
N	VM	4/24/2034	10.90	77.91	17644	15.17	2
N	VM	1/9/2036	9.87	142.66	39285	13.09	2
N	VM	4/28/2030	15.18	145	14138	10.35	1
N	VE	7/8/2030	14.69	143	110986	9.98	1
N	ME	1/17/2031	14.27	104.26	29421	10.84	1
N	VM	4/24/2031	14.13	64	11854	8.89	1
N	VM	8/18/2031	13.98	117	23342	10.19	1
N	ME	9/15/2032	13.27	108.61	31302	12.24	1
N	VM	5/9/2033	12.36	41.97	23892	11.70	1
N	VM	10/17/2033	11.25	131.36	48013	11.70	1

A.3.2 $V_\infty > 18\ km/s$, $C3 < 50\ km^2/s^2$, and Convective Heating Rates $> 8000\ W/cm^2$

Comparison to Girija, et al. [23] results of $V_\infty > 18$ km/s and $C3 < 50$ km/s.

Ice Giant	**AGAs**	**Earth Dep. Date**	**TOF (years)**	$C3\ (\frac{km^2}{s^2})$	$q_{c_{max}}\ (\frac{W}{cm^2})$	**Arrival** $V_\infty(\frac{km}{s})$	**TCW(°)**
N	VM	3/29/2036	8.87	41.59	20857	18.78	2+
N	VE	11/9/2037	7.32	30.51	43871	22.5	2+
N	VM	1/2/2038	7.29	36.93	46012	22.45	2+
N	VE	6/20/2036	8.94	26.60	113192	18.63	2+
N	VM	6/28/2036	9.14	46.87	20220	18.42	2+
N	VV	8/3/2037	8.18	46.36	98030	22.79	2+

Bibliography

[1] *Visions and Voyages for Planetary Science in the Decade 2013-2022*. National Academies Press, 2011.

[2] *Origins, World, and Life: A Decadal Strategy for Planetary Science and Astrobiology 2023 - 2032*. National Academies Press, 2022.

[3] Soumyo Dutta. Aerocapture as an enhancing option for ice giants missions. Technical report, NASA Langley Research Center, 2021.

[4] Angus D. Mcronald and James E. Randolph. Hypersonic maneuvering to provide planetary gravity assist. 1990.

[5] J. Sims, J. Longuski, and M. Patel. Aerogravity-assist trajectories to the outer planets and the effect of drag. *Journal of Spacecraft and Rockets*, 37(1), 2000.

[6] J. D. Anderson, M.J. Lewis, A. P. Kothari, and S. Corda. Hypersonic waveriders for planetary atmospheres. *Journal of Spacecraft and Rockets*, 28(4), 1991.

[7] D. Izzo. Revisiting lambert's problem. *Journal of Guidance, Control, and Dynamics*, 2014.

[8] M. Carney and E. Haddox. Nasa launch services program performance website, 2022.

[9] The MathWorks Inc. Global optimization toolbox, 2023.

[10] The MathWorks Inc. Global optimization toolbox version: 4.6 (r2021b), 2022.

[11] G. Henning, P. Edelman, and J. Longuski. Design and optimization of interplanetary aerogravity-assist tours. *Journal of Spacecraft and Rockets*, 51(6), 2014.

[12] F. A. Lohar, D. Mateescu, and A. K. Misra. Optimal atmospheric trajectory for aero-gravity assist. *Acta Astronautica*, 32(2), 1994.

[13] N. X. Vinh, A. Buseman, and R. D. Culp. *Hypersonic and Planetary Entry Flight Mechanics*. The University of Michigan Press, Ann Arbor, Michigan, 1803.

[14] A. Mazzaracchio. Uncertainties and radius tracking in flight-path angle guidance for aerogravity-assist. *Celestial Mechanics and Dynamical Astronomy*, 2022.

[15] J. Casoliva, D. Lyons, A. Wolf, and K. Mease. Robust guidance via a predictor-corrector algorithm with drag tracking for aero-gravity assist maneuvers. *AIAA Guidance, Navigation, and Control Conference and Exhibit*, 2008.

[16] J. D. Anderson. *(Hypersonic and High Temperature Gas Dynamics)*. American Institute of Aeronautics and Astronautics, 2 edition, 2006.

[17] J. Samareh. A multidisciplinary tool for systems analysis of planetary entry, descent, and landing (sape). 2009.

[18] *NASA 2012 Thermal Fluids Analysis Workshop, Lecture 1: Stagnation Point Heating*, 2012.

[19] Peter Edelman and James Longuski. Optimal aerogravity-assist trajectories minimizing total heat load. *Journal of Guidance, Control, and Dynamics*, 40:1–5, 04 2017.

[20] Ernest R. Hillje. Entry flight aerodynamics from apollo mission as-202. Technical report, NASA Manned Spacecraft Center, 1967.

[21] Mark F. Schoenenberger, McNeil Cheatwood, and Prasun N. Desai. Static aerodynamics of the mars exploration rover entry capsule. *American Institute of Aeronautics and Astronautics*, 2005.

[22] Athul P. Girija, Sarag J. Saikia, James M. Longuski, and James A. Cutts. Amat: A python package for rapid conceptual design of aerocapture and atmospheric entry, descent, and landing (edl) missions in a jupyter environment. *Journal of Open Source Software*, 6(67):3710, 2021.

[23] A. P. Girija, S. J. Saikia, J. M. Longuski, S. Bhaskaran, M. S. Smith, and J. A. Cutts. Feasibility and performance analysis of neptune aerocapture using heritage blunt-body aeroshells. *Journal of Spacecraft and Rockets*, 57(6), 2020.

[24] Alec J. Mudek. 50-year catalogs of uranus trajectory options with a new python-based rapid design tool. 2022.

[25] *Overview of Heatshield for Extreme Entry Environment Technology (HEEET) Project*. 16th International Planetary Probe Workshop (IPPW), 2018.